

12-1-2014

## Designing a Biomimetic Testing Platform for Actuators in a Series-Elastic Co-contraction System

Ryan Tyler Schroeder

University of Nevada, Las Vegas, [ryan.schroeder@unlv.nevada.edu](mailto:ryan.schroeder@unlv.nevada.edu)

Follow this and additional works at: <https://digitalscholarship.unlv.edu/thesesdissertations>



Part of the [Artificial Intelligence and Robotics Commons](#), [Biomechanical Engineering Commons](#), [Biomedical Devices and Instrumentation Commons](#), and the [Robotics Commons](#)

---

### Repository Citation

Schroeder, Ryan Tyler, "Designing a Biomimetic Testing Platform for Actuators in a Series-Elastic Co-contraction System" (2014). *UNLV Theses, Dissertations, Professional Papers, and Capstones*. 2296. <https://digitalscholarship.unlv.edu/thesesdissertations/2296>

This Thesis is protected by copyright and/or related rights. It has been brought to you by Digital Scholarship@UNLV with permission from the rights-holder(s). You are free to use this Thesis in any way that is permitted by the copyright and related rights legislation that applies to your use. For other uses you need to obtain permission from the rights-holder(s) directly, unless additional rights are indicated by a Creative Commons license in the record and/or on the work itself.

This Thesis has been accepted for inclusion in UNLV Theses, Dissertations, Professional Papers, and Capstones by an authorized administrator of Digital Scholarship@UNLV. For more information, please contact [digitalscholarship@unlv.edu](mailto:digitalscholarship@unlv.edu).

**DESIGNING A BIOMIMETIC TESTING PLATFORM FOR ACTUATORS IN  
A SERIES-ELASTIC CO-CONTRACTION SYSTEM**

By

Ryan Schroeder

Bachelor of Science in Mechanical Engineering  
University of Nevada, Las Vegas  
2013

A thesis submitted in partial fulfillment  
Of the requirements for the

Master of Science in Engineering – Mechanical Engineering

Department of Mechanical Engineering  
Howard R. Hughes College of Engineering  
The Graduate College

University of Nevada, Las Vegas  
December 2014



We recommend the thesis prepared under our supervision by

**Ryan Schroeder**

entitled

**Designing a Biomimetic Testing Platform for Actuators in a Series-Elastic Co-Contraction System**

is approved in partial fulfillment of the requirements for the degree of

**Master of Science in Engineering - Mechanical Engineering**  
**Department of Mechanical Engineering**

David Lee, Ph.D., Committee Co-Chair

Brendan O'Toole, Ph.D., Committee Co-Chair

Mohamed Trabia, Ph.D., Committee Member

Hui Zhao, Ph.D., Committee Member

Edward Neumann, Ph.D., Graduate College Representative

Kathryn Hausbeck Korgan, Ph.D., Interim Dean of the Graduate College

December 2014

## **Abstract**

### **DESIGNING A BIOMIMETIC TESTING PLATFORM FOR ACTUATORS IN A SERIES-ELASTIC CO-CONTRACTION SYSTEM**

By  
Ryan Schroeder

Dr. David Lee, Examination Committee Chair  
Professor of Biology  
University of Nevada, Las Vegas

Actuators determine the performance of robotic systems at the most intimate of levels. As a result, much work has been done to assess the performance of different actuator systems. However, biomimetics has not previously been utilized as a pretext for tuning a series elastic actuator system with the purpose of designing an empirical testing platform. Thus, an artificial muscle tendon system has been developed in order to assess the performance of two distinct actuator types: (1) direct current electromagnetic motors and (2) ultrasonic rotary piezoelectric motors. Because the design of the system takes advantage of biomimetic operating principles such as co-contraction in an agonist-antagonist configuration, it exists as an ideal system for testing different actuators for implicit performance attributes that may or may not come closer to the physiological performance of biological muscle.

In order to assess the respective performances of the two actuator types, error and system efficiency were both measured simultaneously in an attempt to characterize the fidelity and efficacy of the force-feedback control system. Although both motor types were shown to perform competitively by torque error, the electromagnetic motors outperformed in terms of efficiency. It is ultimately concluded that either actuator type

may perform more impressively than the other when operating under the appropriate context of application. Specifically, it remains the interpretation of this study that piezoelectric motors require a stiffer elasticity as well as an extremely fast controller frequency in order to fully take advantage of its ultra-fast response time characteristic for torque control.

## **Acknowledgments**

There exists a deep reservoir of reverence for a number of individuals who have helped to sculpt my character and nuance as an engineer, a researcher, and an individual. To those, I say “Thank you.” Specifically, I am in debt to my thesis committee, comprising of the following: Dr. Brendan O’Toole, Dr. Mohamed Trabia, Dr. Hui Zhao, and Dr. Edward Neumann. I am deeply grateful for their time that was dedicated to my project.

Another group of people to whom I feel much gratitude towards is my lab. Lexi Crisp, Kit Knight, Clinton Barnes and Mike Isaacs are individuals who have spent many hours listening to me soundboard ideas off of them and struggling through the challenges of designing a biomimetic, engineering system. To that end, I am very appreciative of their support and advice throughout.

In particular, I am extremely thankful for the effort, time and wisdom that Dr. David Lee has invested not only in my thesis project, but also in my personal development as a professional researcher. I am greatly indebted to his willingness to welcome me into the LoCB (Lab of Comparative Biomechanics).

Finally, I would like to express my gratitude for the support of my friends and family. Brandon Schroeder, Meredith Schroeder, Kathy Schroeder, Roy Schroeder, Mandy Tillitson, Caroline O’Donnell and Sarah Trabia have all comprised of an amazing support system throughout this process.

## Table of Contents

Abstract.....	iii
Acknowledgments.....	v
List of Tables .....	viii
List of Figures.....	ix
Chapter 1: Introduction.....	1
1.1 Overview.....	1
Chapter 2: Robotic Testing Platform .....	5
2.1 Background.....	5
2.1.1 Artificial Muscle-Tendon Systems.....	5
2.1.2 Series Elastic Actuators .....	7
2.2 Design Foci in Biomimetics.....	9
2.2.1 Design Overview .....	9
2.2.2 Series Elastic Actuators in an AMTS.....	13
2.2.3 Co-Contraction .....	16
2.3 Control System.....	20
2.4 System Parameter Tuning.....	28
2.4.1 Elasticity: Allometric Scaling and Springs Selection.....	28
2.4.2 Mass Moment of Inertia .....	34
2.4.3 Damping Effects and Modeling the Passive System .....	35
2.4.4 Tuning the Damped Resonant Frequency for Testing Purposes .....	40
2.4.5 Tuning Controller Gains.....	43
Chapter 3: Performance Evaluation of Actuators .....	48
3.1 Actuator Comparisons .....	48
3.1.1 Electromagnetic Motors .....	48
3.1.2 Piezoelectric Motors .....	50
3.1.3 Choice of Specific Actuators for Artificial Muscle.....	56
3.2 Testing Protocol, Results and Discussion.....	58
3.2.1 Methods .....	58
3.2.2 Results: Overview.....	72
3.2.3 Condition Number Trends.....	76
3.2.4 Trends at Biological Relevance.....	79
Chapter 4: Conclusions and Future Work.....	85
4.1 Conclusions.....	85
4.1.1 Robotic Testing Platform.....	85
4.1.2 Performance Evaluation of Actuators.....	85
4.2 Future Work .....	86

Appendix: Sample Data .....	88
Bibliography .....	90
Curriculum Vitae .....	92



## List of Tables

Table 1: Design diagram legend .....	13
Table 2: Summary of transducers .....	22
Table 3: DAQ hardware.....	22
Table 4: Controller block diagram legend .....	27
Table 5: Summary of spring constants.....	34
Table 6: Summary of damping coefficients.....	40
Table 7: Summary of mass moment of inertia and resulting resonant frequencies .....	43
Table 8: Summary of master gains used during experimentation.....	47
Table 9: Motor specifications table.....	57
Table 10: Auxiliary hardware .....	58
Table 11: Testing parameter combinations.....	60
Table 12: Miro camera settings.....	62

## List of Figures

Figure 1: Design diagram, labeled (bottom) and not labeled (top).....	12
Figure 2: Series elastic actuator diagram .....	16
Figure 3: Co-contraction diagram for CCW rotation (top) and CW rotation (bottom) ....	18
Figure 4: Control system sensors, Futek torque transducer (left) and Futek tension transducer (right) .....	21
Figure 5: Torque controller block diagram (top) and tension controller block diagram (bottom) .....	26
Figure 6: Allometric curves for scaling muscle-tendon properties (Pollock and Shadwick, 1994).....	30
Figure 7: Oscillating spring-mass model for testing spring constants .....	31
Figure 8: Spring constant test results .....	33
Figure 9: SolidWorks mass moment of inertia model .....	35
Figure 10: Model of the passive system .....	36
Figure 11: Free body diagram of the passive system.....	37
Figure 12: Low force-velocity ratio .....	49
Figure 13: High force-velocity ratio .....	51
Figure 14: Cross-section of a piezoelectric motor .....	54
Figure 15: Piezoelectric motor diagram demonstrating a traveling wave .....	54
Figure 16: Piezoelectric motor choice (left) and geared DC motor (right).....	58
Figure 17: Matlab tracking function example.....	70
Figure 18: All-inclusive data results .....	73
Figure 19: Torque error results per condition number .....	76
Figure 20: Torque error results relative to the EM .....	77
Figure 21: Torque error results at condition three .....	79
Figure 22: Efficiency results at condition three .....	81

Figure 23: Sample data of the electromagnetic motor at condition three ..... 88

Figure 24: Sample data of the piezoelectric motor at condition three ..... 89

## **Chapter 1: Introduction**

### 1.1 Overview

The need to develop robotic actuator systems, which can mimic and even exceed the performance of biological muscle, has long been stressed (Hollerbach et al., 1992). Although there has been much progress in recent years, conventional actuators still fall dramatically short of such an ambitious goal. Therefore, a new actuator design is proposed in order to assess the performance of two different motor types, namely the following: (1) DC electromagnetic motors (EM) and (2) ultrasonic rotary piezoelectric motors (PM).

Although there are multiple parameters, which could be measured in order to assess the performance of different actuators, this research proposes the specific evaluation of torque error and system efficiency. By approaching the characterization of actuator performance with these two measures, a thorough insight should be accessible within the context of a biomimetic artificial muscle-tendon system.

Although there exists a multitude of actuator types, it remains unsurprising that the main body of robotics actuation research has been inadequate in competing with the organic machinery of biological organisms. After billions of years, biology has fine-tuned an extremely impressive actuator. As a result, muscle is soft, contractile and dense with power. In addition, it can boast great efficiencies and has force/elastic memory characteristics. At the heart of these attributes is a fundamental operating principal, which can only be described as a ratcheting mechanism. Under the context of a sliding filament, actin and myosin perform cross-bridge cycling and pull on each other, allowing the

muscle to exert a linear contractile force in bulk. This process is fundamentally at ends with an EM that uses magnets in order to incite rotational force, or torque, about a rotor. However, PM's also utilize a ratcheting mechanism, similar to that of muscle, in order to actuate motion. Thus, a biomimetic artificial muscle-tendon system (AMTS) has been designed in order to test and compare the performance characteristics of these two motors within the context of biomechanical function.

In order to design a biomimetic AMTS, the physiology of the biological system is assessed and categorically prioritized into descending characteristics of importance. Muscle itself is arguably the most important element in the system. As stated above, this comparative study will look to EMs and PMs in order to compare their respective performances. However, another important observation identifies the muscle-tendon system as a series elastic actuator. These systems are essentially characterized by a force transmission to a load with an elastic element (e.g. tendon or spring) configured serially and in between the actuator and the load. This allows for a high-fidelity force control (given predictable deflections of the elastic element) as well as a broad dynamic range resulting from the capability of compliance to filter out chatter and unwanted vibrations. For these reasons a serial elastic configuration was designed for the robot. Although the benefits of series elastic actuators have already been demonstrated in many studies (Robinson et al., 1999; Pratt and Krupp, 2004), biomimetics has not yet been explored explicitly under the context of physiologically relevant parameter tuning (e.g. tendon elasticity, oscillation frequency, etc.).

Besides the fact that a muscle-tendon system essentially behaves as a series elastic actuator, another important characteristic remains that of co-contraction. This means that

at any given time, two or more muscles may be pulling against each other about a joint. This particular design quality gives the system more flexibility and control over the net forces/torques to be asserted. Thus, the artificial muscle design incorporates two independent series elastic actuators in order to transmit a net torque about a central revolute joint while at the same time maintaining active levels of co-contraction.

In order to assess the performance of EMs and PMs in the artificial muscle tendon system described in this document, a simple sinusoidal torque profile will be provided to the control system. This waveform will be prescribed to the system at various frequencies relative to the damped resonance of the system. Additionally, springs of varying elasticity will be applied to the system. An allometric analysis (Pollock and Shadwick, 1994) of tendon properties (e.g. cross-sectional area, resting length, etc...) was conducted by scaling motor torque to a biologically relevant body mass and consequentially, tendon properties. This analysis resulted in a relatively stiff spring. Thus, three different springs ranging from softer to stiffer (i.e. the stiffest being the most analogous to biological tendon) will be applied to the system. All trials will be tested with co-contraction levels relative to the maximum net-torque-inducing tension in the line (33%), which has been shown to occur in unpredictable biomechanical activities such as height landings (Yeadon et al., 2009).

A relevant evaluation of actuator-specific performance will include error and system efficiency analysis. Here, error is defined as the difference between a prescribed torque/tension input to the controller and a measured torque/tension output via force transducers in the system. Current will also be measured in order to calculate electrical energy consumption so that it may be compared with mechanical output energy for an

analysis of system efficiency. By evaluating the system based on error and efficiency, the question of implicit force control and fidelity can be addressed under the context of a ratchet-based actuator as compared to an electromagnetic actuator.

It should be noted that this document is laid out in a manner described throughout this paragraph. The organization is partitioned into four main chapters, the first of which comprises the current introduction. Chapter 2 describes the robotic testing platform, which was designed and built for this study. A thorough background and literature review is presented in sections 2.1 and 3.1. These include the subtopics of artificial muscle tendon systems, series-elastic actuators and motor comparisons (e.g. DC electromagnetic motors and piezoelectric motors). A description of general design foci is presented under the context of biomimetic function via sections 2.2 and 2.3 and it includes series-elastic actuators, co-contraction and the control system. Section 2.4 comprises of testing procedures utilized for the purposes of tuning different system parameters such as elasticity, mass moment of inertia, viscous damping, damped resonant frequencies and controller gains. Chapter 3 shifts the topic of focus from the robotic testing platform to the methodology and testing of different actuator types in a frequency domain. Finally, Chapter 4 summarizes the collective body of work with respect to the robotic testing platform as well as the specific motor study that was conducted. This summary depicts many of the most vital takeaway points as well as the potential of future work on this research.

## **Chapter 2: Robotic Testing Platform**

### **2.1 Background**

#### **2.1.1 Artificial Muscle-Tendon Systems**

The concept of an artificial muscle is not a new one. In fact, perhaps the most famous and widely used artificial muscle was originally invented in 1958. Richard H. Gaylord developed the actuator now most commonly referred to as the McKibben artificial muscle. In the early 1960s, Joseph L. McKibben popularized the device by applying it to a wheel chair system for his paralyzed daughter, in an effort to restore some of her mobility and independence. However, the diversity of application did not stop there, and in the past several decades there has been much research (Klute et al., 1999; Tondu, 2012). on the various innovations of the McKibben muscle.

Basically, its structure comprises of an inflatable bladder, which is sheathed with a double helical weave. By modulating the pressure of compressed gas inside of the bladder, it expands radially and contracts lengthwise. Although much of the design of the McKibben muscle seems obscure and at ends with the specific nature of biological muscle from an intuitive perspective (certainly muscle is not a pressurized gas), nonetheless, the driving point is that of contractile length actuation. In fact, it has been shown empirically that the McKibben muscle stands up to the task of biomimetic function in terms of its force-length relationships compared to that of biological muscle. However, it falls short at mimicking the characteristic force-velocity relationship that muscle so distinctly exhibits (Klute et al., 1999). Nevertheless, the McKibben muscle has certainly stood the test of time and thusly, it is used here as a characteristic example defining what is required of an artificial muscle at the most fundamental level. Again, the



fact that the McKibben muscle behaves as a contractile length actuator describes the most crucial distinction.

Given this qualification for an artificial muscle, it remains a fair question to ask if a rotary motor can ever truly be considered an artificial muscle. Certainly, the concept of rotation as the dynamic output of an actuator seems at odds with that of length contraction. However, a rotary motor may be coupled with a linear transmission in order to produce length contraction. In the research of current topic, 3D-printed plastic (ABS) spools were coupled to the motor shafts of electromagnetic motors and piezoelectric motors in order to instigate linear motion of a filament wrapping around the spool.

It is important to note that this not only allows for length contraction at the filament but it also imposes a mechanical limitation in terms of how force can be transmitted from the actuator to the output of the system. This is to say that a filament can only transmit tension force and not compressive force. This particular attribute reflects the nature of a muscle-tendon unit in that both muscles and tendons can only interact through tension force. It should be noted that biological muscle is capable of lengthening, but only passively, by means of an external force (e.g. gravity) or a co-contractive muscle opposing its direction of action.

Another characteristic of a muscle-tendon system is that of compliance in the tendon. In other words, a tendon is capable of relative displacement under tension and can return the energy of that displacement with very little hysteresis. Basically, the tendon acts as a linear spring. Thus, the relatively rigid filament wrapping around the spools on the motors is connected to a spring in series in order to give the design some

compliance. With these characteristics in place, the distinction of an artificial muscle-tendon system (AMTS) is clear. Also, it should be noted that the configuration of an actuator in series with an elastic element is commonly called a series elastic actuator. This topic will be discussed more thoroughly in the following sub-section (2.1.2).

### **2.1.2 Series Elastic Actuators**

Series elastic actuators (SEA) have found their way into robotics research largely over the past twenty years (Pratt and Williamson, 1995). Prior to this, the mentality of “the stiffer the better” was thought to be superior in terms of force transmission. However, researchers have recently shown that many of the limitations of elastic transmissions can be overcome and in fact, the benefits of elastic force transmission can far exceed that of its rigid counterpart (Pratt et al., 1995). This is especially true under the context of locomotive robots, where smooth force control is vital to a stable mechanical interaction with rough terrains.

Not only have SEAs been proven in terms of their performance in isolated systems, but they have also been introduced into more complicated systems such as robotic organisms and exoskeletons (Pratt and Krupp, 2004; Veneman, 2006). As a result, great promise has been shown at the whole system level. Again, smooth force transmission provides a reliable and consistent quality benefitting the performance of force feedback in the control systems of such machines.

One of the limitations undermining smooth force transmission in a rigid design is that of chatter, or excessive vibration. However, by placing a compliant component

(usually a spring) serially in between the actuator and the output of a given system, the compliance acts as a mechanical filter to the noise of vibration. Because most springs tend to exhibit very little hysteresis, nearly all energy gets returned to the device, including the vibrations it absorbs. However, there is also a time lag associated with the input of a given vibration and the output of that energy back into the system. As a result, the output of this noise is much smoother since it may be dispersed over a longer period of time. In other words, the noise's energy is conserved, but its power is dissipated.

Clearly, the spring is the defining element of an SEA relative to a rigid actuator system. As such, a large portion of research regarding these systems has focused on tuning the spring for optimal performance. In fact, appropriately tuned springs have been shown to help alleviate some of the adverse qualities of actuators such as DC motors and drives such as gear trains or belt drives. Specifically, higher spring constants can be shown to increase force bandwidth and lower spring constants can be shown to minimize stiction (i.e. static friction) and impedance (Robinson et al., 1999). Although many different actuators have been utilized for SEAs, piezoelectric motors have not yet been applied to such systems. This is likely because piezoelectric motors are not commonly thought of in the context of force feedback systems. Thus, the current topic of research intends to address this unexplored novelty. This subject will be explored more thoroughly in Chapter 3.

## 2.2 Design Foci in Biomimetics

### 2.2.1 Design Overview

The outlook perspective of design functionality dominated as a key component for consideration and continues to hold much sway in terms of the research described in this document. Not only was it required of the AMTS described to be an effective actuator system, but specifically the manner and strategy for actuation was determined a crucial attribute for biomimetic application. In other words, there are many ways to build a capable actuator system, but only a few ways to do so in a manner that reflects the biology of a muscle tendon system. Thus, a subtle balance must be drawn between designing a robust, capable machine and simultaneously prioritizing the most vital and fundamental attributes of the desired biology. The following paragraphs will describe and explain some of the key design realizations utilized for the most current iteration of this project. However, the specific points of biomimetic design will be left for discussion in future sections of this chapter.

Perhaps the most eye-catching feature of the AMTS is that of its load wheel. This particular component of the device acts as a baseline mass moment of inertia (MoI) to which, the actuators are designed to pull in rotation. In the biological analogy, the load wheel may be thought of as a body segment in rotation (e.g. a foot). The load wheel is bolted to a 3D-printed plastic (ABS) rail system that allows for additional 2.5lb weights to be added for increased loading. The load wheel is also mounted to a uni-axis torque transducer (Futek) on its underside. This torque transducer is assembled such that it can measure the reaction torque at the load wheel. It is also fixed to an aluminum plate

underneath it. The aluminum plate helps to isolate the transducer from mechanical noise and any relative motion seen beneath it.

Beneath the aluminum plate, an aluminum tube (outer diameter = 5/16") acts as a center support for the torque transducer and the load wheel. It is also encompassed by a 3D-printed triple-spool. This triple spool is utilized as part of a force transmission relying on two rigid filaments wrapping around the troughs of the spool. Thus, as tension forms in the filaments, rotation is incited about the spool and consequently, the tube, the transducer and the load wheel. It should be noted that the triple-spool was originally a double-spool. However, due to the continual force-couple resulting from one point of force contact hanging directly above the other, one of the filaments (the right side) was split into two at a "y" junction. Thus, the rogue moment was eliminated and the design was stabilized.

Beneath the center spool, the aluminum tube continues into a structural housing where two ball bearings allow for axial rotation about the tube. This revolute joint may be thought of similarly to a hinge joint in biology (e.g. an ankle). The structural housing of the joint is bolted to a rigid 80/20 aluminum structure that is mounted to the wall. Given the assumption of relatively low reaction forces at structural attachments, the 80/20 mounts are likely overbuilt in terms of support. Regardless, it acts as a grounded fixture necessary in allowing for the negligibility of any structural effects such as swaying, bending or twisting.

From the center spool, the rigid filaments extend outward toward the outer extremes of the design. On the right side, the lowest and highest filaments are both

attached to a 3D-printed “y” junction. On the opposing side of the “y” junction, another filament attaches to an inline tension transducer (Futek). The left-side filament directly attaches to an identical tension transducer. These instruments are designed to measure the tension in the filaments, as well as everything else in series with the lines. The tension transducers may be considered analogous to Golgi tendon organs in biology. This functionality will be discussed further in future sections of this chapter.

Immediately distal to the tension transducers, linear extension springs are attached in series. These springs may be thought of as artificial tendons, capable of force transmission via tension and allowing for a predetermined compliance. Finally, a last piece of filament attaches the extension springs to two more single-spools on both sides of the actuator system. These single-spools allow for the filament to be wrapped around. They are also rigidly mounted via a setscrew at the rotary shafts of the motors just beneath. The motors themselves may be thought of as artificial muscles in the system. They are fixed to small sections of aluminum box beams, which are in turn bolted to the main 80/20 support frame. The main support frame may be thought of as a rigid skeletal structure that comprises the body of the entire system. An image displaying the design in full can be viewed below, both unlabeled and labeled (see Fig. 5 and Table 1)

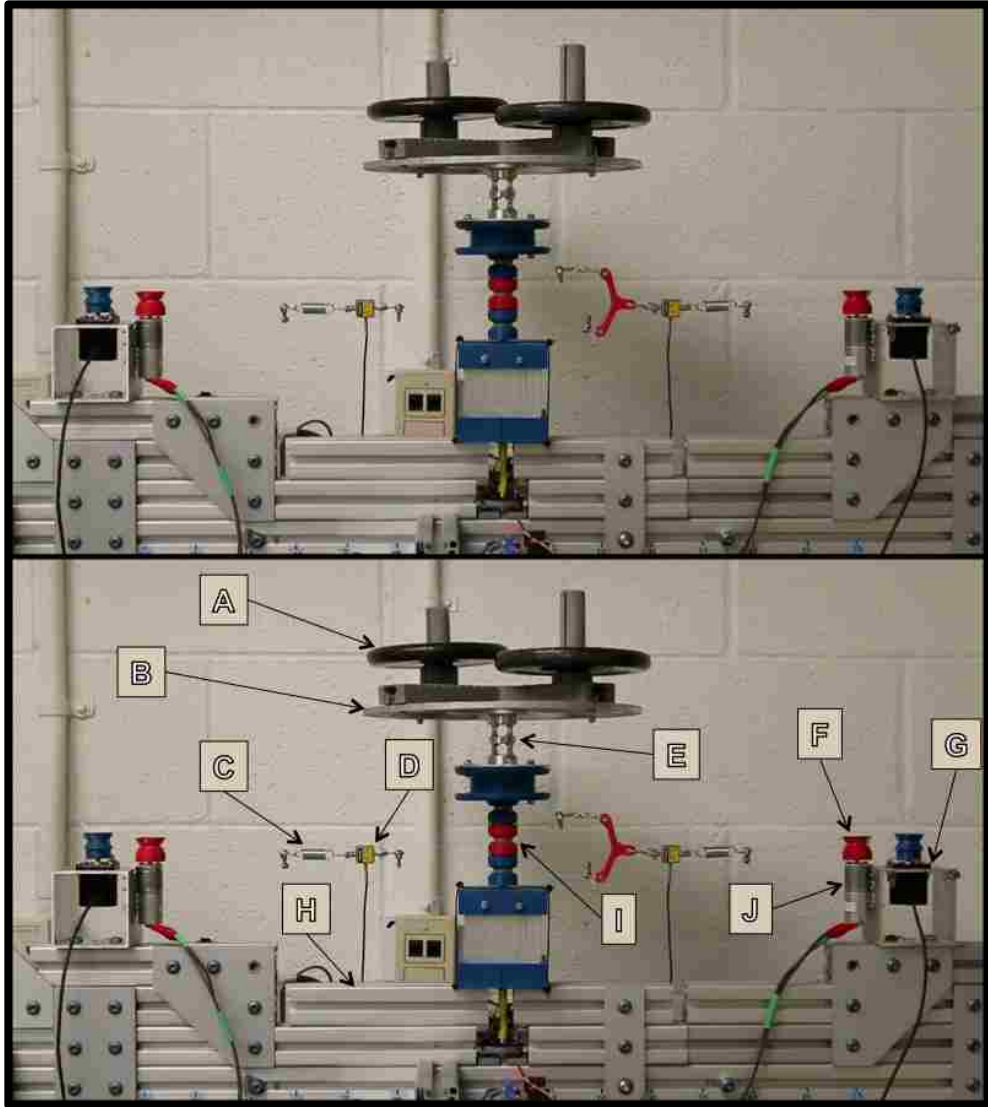


Figure 1: Design diagram, labeled (bottom) and not labeled (top)

Table 1: Design diagram legend

<b>Design Diagram Legend</b>	
Label	Description
A	Variable Mass Moment of Inertia
B	Load Wheel
C	Extension Spring (i.e. robotic tendon)
D	Tension Transducer (Futek)
E	Torque Transducer (Futek)
F	3D-Printed Plastic (ABS) Spool
G	Piezoelectric Motor (DTI PM-20R)
H	Rigid Aluminum 80/20 Mount
I	Revolute Joint
J	Electromagnetic Motor (Pololu Micro Metal Gearmotor)

The description provided in this section communicates a general overview of the actuator system, which was developed during the design phase of this research. The remainder of section 2.2 will delve into many of the specific foci, which were deemed the most appropriate in mimicking biomechanical function. Specifically, the following points will be discussed: (1) series elastic actuators as artificial muscle-tendon units (sub-section 2.2.2) and (2) co-contraction in a flexor-extensor system (sub-section 2.2.3).

### 2.2.2 Series Elastic Actuators in an AMTS

In order to incorporate a series elastic actuator (SEA) into the design of an artificial muscle tendon system, it is important to first recognize the analogous elements of this design configuration. Specifically, these elements mainly comprise of the following: (1) an actuator (e.g. motor) → biological muscle, (2) some elastic element



(e.g. spring) → biological tendon and (3) a force (tension) transducer → Golgi tendon organ.

It should be noted that an SEA does not technically necessitate a tension transducer, however this is one typical solution for introducing force feedback into the system. Often times, the length change of a spring can also be used for force feedback by taking advantage of Hooke's Law.

Regardless of control sensors, the most fundamental interaction of an SEA remains the transfer of force from the actuator to the spring element. In the specific case of this AMTS, either an electromagnetic or a piezoelectric motor is used to wind a rigid filament around a 3D-printed plastic (ABS) spool in order to provide tension to its respective spring. The serial nature of this configuration guarantees a common tension felt throughout the line connecting the motor to the spring. However, this also implies that relative displacement between the two elements is non-uniform. Again, it is this relative displacement that is commonly used for measuring the tension resulting from the motor. However, placing a tension transducer in the same line eliminates a step from this calculation by directly measuring tension. Again, because tension is uniform in the line, the tension felt by the transducer is the same tension that the spring feels as well as the linear load acting on the motor through the radius of the spool and the actuation load acting on the center support tube via the radius of the center spool. The following equations describe the load on the motor and the actuation force pulling on the center spools in terms of the line tension:

$$\tau_{load} = T_{tot} * R_{ss}$$

$$\tau_{LW} = T_{tot} * R_{cs}$$

In the above equations,  $\tau_{load}$  → the torque load being felt by the motor,  $T_{tot}$  → the total tension in the line,  $R_{ss}$  → the radius of the side spool (0.01m),  $\tau_{LW}$  → the torque at the load wheel and  $R_{cs}$  → the radius of the center spool (0.01m). Because  $R_{cs} = R_{ss}$  this means that the torque at the load wheel essentially is the load at the motor. This also means that there is a one to one gearing ratio between the motor and the output of the load wheel. Thus, ideally, any torque or rotational velocity of the motor should directly be transferred to the output at the load wheel. Of course, in actuality, there are always two actuators acting on the center spool at all times. As a result, the output is the superposition of both motors at any given time.

In terms of force feedback, the inline tension transducers are very similar to Golgi tendon organs in biology, which are connected to the tendon and muscle in series. When the muscle exerts a tension on the tendon, this same tension tightens strands of collagen that wrap around the afferent type Ib sensory nerve fibers making up the organ. The action potential frequency of the resulting nerve impulse via tension stimulation signals the force being developed over approximately 10 or 20 motor units within the muscle. This signal is representative of the whole muscle force. The motor control system interprets this signal and regulates activities such as the transitions between stance and swing phases in the locomotion of certain animals (Conway et al., 1987).

The following image (see Fig. 7) highlights both series elastic actuators while they are assembled in the system.

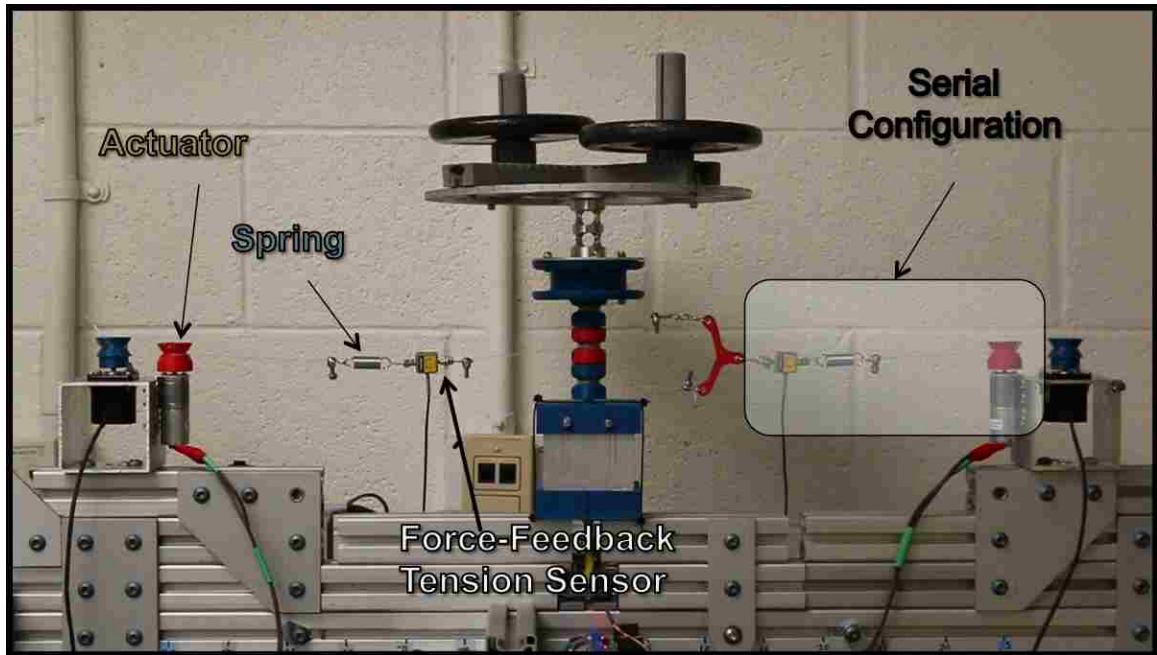


Figure 2: Series elastic actuator diagram

It should be noted that a rigid filament in series with an extension spring was chosen specifically and intentionally as an artificial tendon. Biological muscle is not capable of actively lengthening, otherwise called eccentric contraction. In fact, muscle can only elongate when its antagonist counterpart (or some other external force e.g. gravity) pulls it back. Similarly, a tendon cannot transmit force via compression, as in a rope, for example. Thus, the rigid filaments of the AMTS mimic this unidirectional behavior of the muscle tendon unit at the SEA level.

### 2.2.3 Co-Contraction

Co-contraction is an important concept in biology. In particular, the actuation of motion about a joint is nearly always regulated by at least two different muscle-tendon

units: an agonist and an antagonist. In biology, the agonist muscle is responsible for rotating some inertia (e.g. a leg segment) about its joint in a given direction, while the antagonist is responsible for opposing that motion in the opposite direction and with some magnitude. This opposing tension force is known as co-contraction. The idea of an agonist-antagonist muscle system should not be confused with the concept of a flexor-extensor system. Generally speaking, a flexor is determined by which muscle folds a respective limb distally inward toward the body, while the extensor unfolds (i.e. extends) the limb. For the purposes of this research the agonist motor is defined as the actuator instigating a net torque, or driving torque, at the load wheel. Adversely, the antagonist artificial muscle opposes the driving torque in order to maintain an active co-contraction in the system. The following image (see Fig. 8) highlights the use of co-contraction in the AMTS of this research.

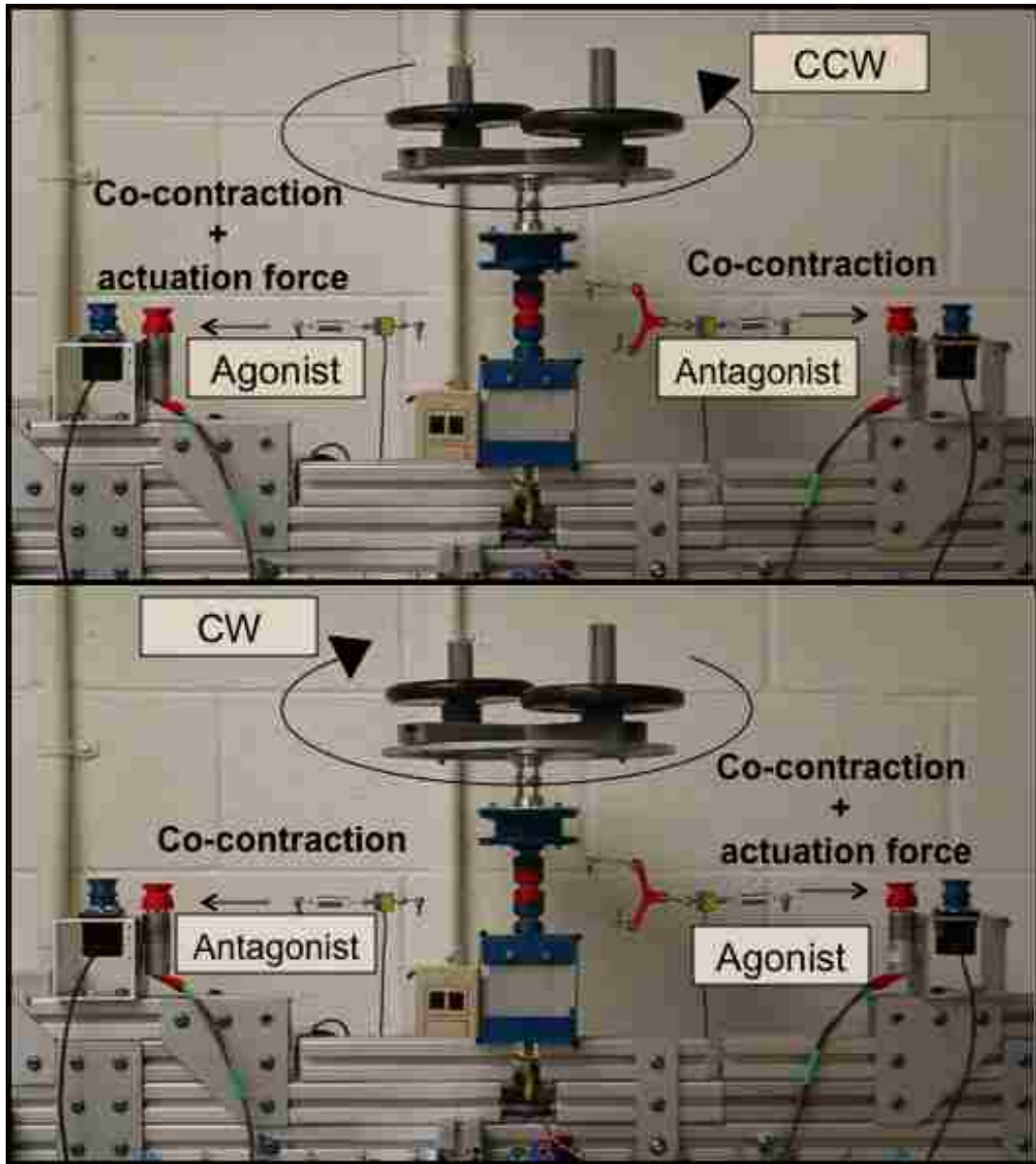


Figure 3: Co-contraction diagram for CCW rotation (top) and CW rotation (bottom)

Although it may seem unintuitive, or even counter-productive to enlist an opposing muscle during co-contraction, there are actually great benefits associated with such a design. While it is true that utilizing an antagonist muscle for co-contraction will add an extra load to its agonist counterpart, it is also true that the added strain felt in the

tendon of the system acts as small potential energy reservoir that may be tapped for extra power as needed. In biology, this usually refers to a perturbation of some type. For example, a human standing on a raised platform can perform a height drop by falling to the ground. When this even occurs, extra co-contraction is employed in order to deal with the sudden perturbation via the normal force of collision (Yeadon, 2010). Effectively, this allows for the human to adjust their musculature in order to quickly stabilize and avoid injury. Essentially, the tendon stores extra energy that is released upon or shortly after the vertical collision with the ground. This allows the muscle-tendon system to do quick work for the goals just mentioned above.

For the purposes of this research, a constant co-contraction was chosen depending on the experimental condition (e.g. torque magnitude). Specifically, the tension in the antagonist's tendon was programmed to 33% of the waveform amplitude  $\tau_{max}$  for each trial. This percentage was chosen as a result of previous research studying co-contraction levels in height droppings (Yeadon, 2010). In order to calculate 33%, torque was first converted into tension at the artificial tendon, via the following derivation:

$$T_{tot} = \frac{\tau_{max}}{R_{cs}} + T_{cc}$$

In the above equation,  $\tau_{max}$   $\rightarrow$  the maximum amplitude of the target waveform,  $T_{cc}$   $\rightarrow$  constant tension in the artificial tendon due to co-contraction,  $T_{tot}$   $\rightarrow$  the total tension in the artificial tendon and  $R_{cs}$   $\rightarrow$  the radius of the center spool (0.01m). Noting that a 33% co-contraction is desired for  $T_{cc}$ , the appropriate substitutions are made:

$$\frac{\tau_{max}}{R_{cs}} + \frac{T_{tot}}{3} = T_{tot}$$

Thus,

$$\frac{\tau_{max}}{R_{cs}} = \frac{2}{3} T_{tot}$$

$$\frac{3}{2} \frac{\tau_{max}}{R_{cs}} = T_{tot}$$

Knowing that:  $T_{cc} = \frac{1}{3} T_{tot}$

We finally get,

$$T_{cc} = \frac{1}{2} \frac{\tau_{max}}{R_{cs}}$$

This equation resulted in tension  $T_{cc}$  values of the following: 0.95, 1.34 and 1.78N, given  $\tau_{max}$  values of 0.019, 0.027 and 0.036 Nm, respectively. Because of the volatile nature of a height dropping in terms of perturbation, this is likely a higher than average amount of co-contraction seen in lower-limb activities typical of humans. However, it was nonetheless chosen in order to help address issues of sudden perturbation between the dual control systems of the AMTS.

### 2.3 Control System

The control scheme of the AMTS is partitioned into two independent subsystems. The primary control is responsible for controlling torque output at the load wheel via the agonist motor, while the secondary control is tasked with modulating tension in the antagonist's tendon (i.e. spring). By controlling tension in the spring opposing net torque about the load wheel, impedance can be utilized for perturbation rejection. In this way,

both motors are simultaneously tasked each with an independent control objective (i.e. two inputs, two outputs).

In order to simultaneously control both net torque about the load wheel and tension in the antagonist motor's spring, three independent force transducers are utilized. For net torque control, a reaction torque transducer (Futek TFF325) (see Fig. 9 and Table 4) is used to measure the instantaneous torque at the load wheel. For tension control, an inline tension transducer (Futek LSB200) (see Fig. 9 and Table 4) is used to measure the instantaneous tension in the opposing spring. Because only the tension on the antagonist side of the load wheel is regulated at a time, only two sensors are utilized simultaneously, while the other tension transducer hangs idly until the motors swap controller schemes.



Figure 4: Control system sensors, Futek torque transducer (left) and Futek tension transducer (right)



Table 2: Summary of transducers

<b>Summary of Transducers</b>							
#	Measurement	Company	Model	Type	Capacity	Overload	Weight
1	reaction torque	Futek	TFF325	Custom Load Cell	0.353 Nm	0.530 Nm	0.065 kg
2	tension and compression	Futek	LSB200	JR S-Beam Load Cell	4.45 N	44.5 N	0.009 kg

Table 3: DAQ hardware

<b>DAQ System</b>			
#	Hardware	Company	Model
1	DAQ Card	National Instruments	PCI-6251
2	Chassis	National Instruments	SCXI-1000DC
3	Terminal Block	National Instruments	SCXI-1321
4	Connector Block	National Instruments	SCXI-1302

Although both controller subsystems have individual objectives, they both utilize a similar controller strategy, which has been well established over several decades of controller research. Specifically, a classic PID (proportional-integral-derivative) controller has been built for each control scheme. Since the PID controller refers to error regulation, it is mathematically defined in the following equation:

$$Error = Target - Actual$$

In the above equation, **Target** → the prescribed target of whichever parameter is being controlled for (e.g. a sine waveform for net torque and a step input at some magnitude, for opposing tension) and **Actual** → the instantaneous measurement of either the torque transducer (Futek) or the inline tension transducer (Futek).

The proportional controller sends a control signal, which is proportional to the error by a constant  $K_p$ , as its name suggests. The integral controller sends a control signal that is proportional by a constant  $K_i$  to the integral of error over the controller time period  $\left(\frac{1}{f_{ctrl}}\right)$  where  $f_{ctrl} = 50\text{Hz}$  for both motor types. It should be noted that a trapezoidal rule algorithm was used to numerically calculate the integration of error in this part of the controller. The differentiator controller sends a control signal that is proportional by a constant  $K_d$  to the change in error over the controller time period described above. It should be noted that a variation of Newton's difference quotient was used to numerically calculate the differentiation of error in this part of the controller. In order to converge all three methods (i.e. P, I and D) into a single, tangible control signal, they were all summed together. The final control signal was scaled by a master gain  $K_m$  in order to approximate a linear conversion from pulse width modulation of voltage input to torque output at the motor. The following equations mathematically describe the controller operations:

$$CS_p = K_p * Error_j$$

$$CS_i = K_i * \int_{t=j-1}^{t=j} Error \, d\tilde{t} \approx K_i * h * \left(\frac{Error_{j-1} + Error_j}{2}\right)$$

$$CS_d = K_d * \frac{d}{dt}(Error) \approx K_d * \left( \frac{Error_j - Error_{j-2}}{2h} \right)$$

$$CS_{tot} = K_m * (CS_p + CS_i + CS_d)$$

In the above equation set,  $CS \rightarrow$  the controller signal,  $K \rightarrow$  the controller gain,  $Error \rightarrow$  the target minus the actual,  $h \rightarrow$  is the time step defined by the inverse of the controller frequency (50Hz),  $t \rightarrow$  time, subscript  $p \rightarrow$  stands for proportional, subscript  $i \rightarrow$  stands for integral, subscript  $d \rightarrow$  stands for derivative, subscript  $m \rightarrow$  stands for master, subscript  $tot \rightarrow$  stands for total, and subscript  $j \rightarrow$  an iteration counter.

The master gain was necessary in compensating for the lack of an established plant or model in the controller. Although, there has been much work performed on modeling the dynamics of electromagnetic motors over the past years (e.g. Krishnan and Pillay, 1989), the modeling of ultrasonic piezoelectric rotary motors has been somewhat sparse. Regardless, there has been some work done in order to characterize the dynamics of these actuators (Sun, 2010). However, these models are extremely complicated and require a very thorough understanding of subtle actuator characteristics, which are simply beyond the scope of this research. It has always been the prime objective of this author to ensure that a fair treatment of each motor type be given, such that an appropriate assessment is possible through the results of this study. Thus, any modeling discrepancies or inaccuracies could easily lead to a biased experimental result in terms of the performance of the respective motors. Thus, it was decided that a carefully tuned PID controller would suffice to control both motor types robustly enough for application, even without a thorough theoretical model of each motor type.

An advantage of the control scheme outlined above is that both motors are constantly utilized to help control the system more effectively, regardless of their agonist/antagonist role. Another way to think of this strategy requires that the agonist motor play a lead role in controlling for net torque about the load wheel while the other motor supports this goal by regulating impedance in the system.

Although this control system implies that either subsystem is completely independent from the other, in reality, there is a very prominent physical interaction between the two. It is important to recognize that not only can the control systems work together, but sometimes they will also struggle against each other in a sequence of “tug-of-war.”

Take for example the antagonist motor tasked with actively maintaining a constant tension in its respective spring. As soon as the agonist motor begins to pull on its spring from the other side of the wheel in order to incite a net torque, the antagonist sees a spike in its tension. This instigates the antagonist motor to follow along with the torque motor in the same direction. In this case, both motors are decidedly working together towards a similar kinematic end goal. However, discord can emerge if/when the antagonist overshoots its goal of constant impedance. This commonly occurs when the agonist motor is approaching a local maximum of its prescribed sine waveform. When this happens, torque is reaching its maximum. This results in a more volatile control phase, with respect to a constant impedance scheme. As a consequence, the antagonist will often overshoot its target. This results in an amplified oscillation that also begins to perturb the net torque control with oscillations. A cascading effect can occur where both motors begin to pull against each other back and forward, resulting in an amplified sense

of overshoot for both control schemes simultaneously. A potential easing to this effect lies in the controller gains. By lowering the respective gains of the controllers, the motors will interact with perturbations less sensitively. In other words, this creates more tolerance for some level of perturbation at the cost of an increase in error. This becomes an important design limitation in terms of gains tuning for the control system. The topic will be expounded upon in sub-section 2.4.5 of this document.

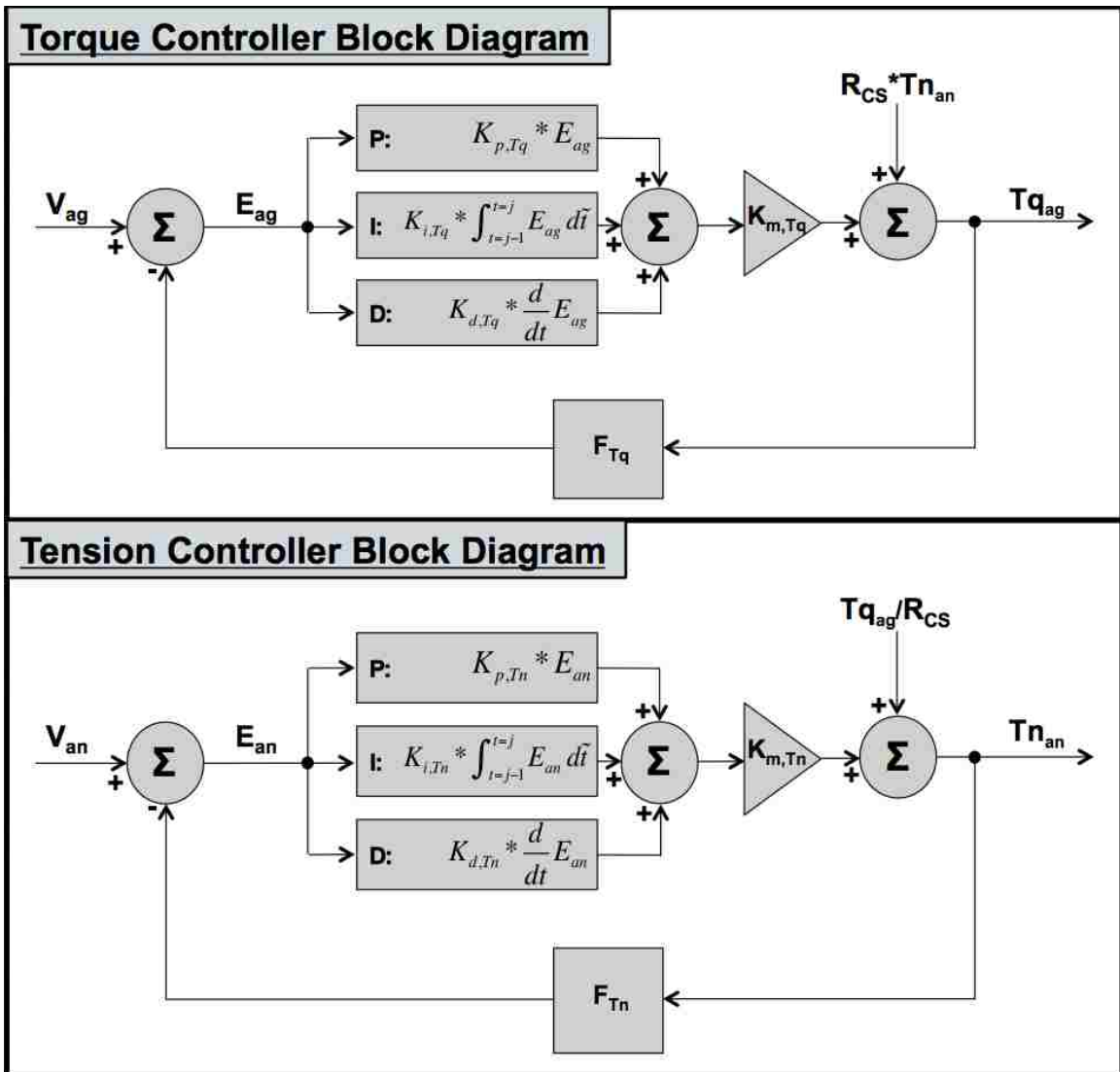


Figure 5: Torque controller block diagram (top) and tension controller block diagram (bottom)

Table 4: Controller block diagram legend

<b>Controller Block Diagram Legend</b>			
<b>Subscript</b>	<b>Description</b>	<b>Symbol</b>	<b>Description</b>
<i>T<sub>q</sub></i>	<b>torque</b>	<i>V</i>	<b>voltage input</b>
<i>T<sub>n</sub></i>	<b>tension</b>	<i>E</i>	<b>error</b>
<i>ag</i>	<b>agonist</b>	<i>K</i>	<b>gain</b>
<i>an</i>	<b>antagonist</b>	<i>T<sub>q</sub></i>	<b>torque</b>
<i>p</i>	<b>proportional</b>	<i>T<sub>n</sub></i>	<b>tension</b>
<i>i</i>	<b>integral</b>	<i>R</i>	<b>radius</b>
<i>d</i>	<b>derivative</b>	<i>F</i>	<b>Futek Transducer</b>
<i>m</i>	<b>master</b>	<i>P</i>	<b>proportional</b>
<i>CS</i>	<b>center spool</b>	<i>I</i>	<b>integral</b>
		<i>D</i>	<b>derivative</b>

## 2.4 System Parameter Tuning

### 2.4.1 Elasticity: Allometric Scaling and Springs Selection

The elasticity of a series elastic actuator is paramount to its performance.

Specifically, the spring constant  $k_{sp}$  is used to characterize this property. It should be noted that Hooke's Law for a linear spring states the following:

$$F = -k_{sp}\Delta x$$

The above equation essentially indicates that force  $F$  is proportional to displacement  $\Delta x$  of the elastic element, or spring. Thus, the primary question considers what an appropriate spring constant should be for an AMTS.

In biology, allometry (i.e. the study of scaling morphology to body size) is commonly used as a predicative tool for modeling different parameters of an animal's body relative to its bulk mass or volume. To accomplish this, a power law equation is utilized in order to characterize this nonlinear relationship. A generalized power law equation has been listed below for the reader's convenience:

$$y = kx^a$$

Or in logarithmic form,

$$\log y = a \log x + \log k$$

In the equations above,  $y \rightarrow$  the desired parameter prediction,  $x \rightarrow$  the known parameter, such as body size or mass,  $k \rightarrow$  the scaling coefficient and  $a \rightarrow$  the scaling exponent.

By utilizing the allometric equations of specific muscle-tendon parameters, a “biologically relevant” spring constant was ascertained. In determining the necessary parameters needed to calculate the spring constant of a tendon, the following equations were formulated:

$$\text{Noting that } \varepsilon = \frac{\Delta l}{l_o} = \frac{\sigma}{E}$$

$$k_{sp} = \frac{F_m}{\Delta l} = \frac{F_m}{\varepsilon_t * l_{o,t}} = \frac{F_m * E_t}{\sigma_t * l_{o,t}} = k_{sp}$$

$$\text{In the above equation, } \sigma_t = \sigma_m \left( \frac{A_m}{A_t} \right)$$

$$\text{Since } F = \sigma A$$

$$\text{And } F_t = F_m \text{ in a serial configuration.}$$

In the above equation set,  $\varepsilon \rightarrow$  strain,  $\Delta l \rightarrow$  a change in length,  $l_o \rightarrow$  the resting length when no tension force is felt,  $\sigma \rightarrow$  stress,  $E \rightarrow$  Young’s Modulus,  $F_m \rightarrow$  the maximum force expected of the artificial muscle (e.g. motor),  $\varepsilon_t \rightarrow$  tendon strain,  $l_{o,t} \rightarrow$  resting length of the tendon,  $E_t \rightarrow$  Young’s Modulus of the tendon,  $\sigma_t \rightarrow$  the tendon stress,  $\sigma_m \rightarrow$  the muscle stress shown to be 0.3MPa (Close 1972; Wells, 1965),  $A_m \rightarrow$  the cross-sectional area of the muscle,  $A_t \rightarrow$  the cross-sectional area of the tendon and  $F_t \rightarrow$  the tension force felt in the tendon.

Allometric curves (Pollock and Shadwick, 1984) were used to identify appropriate values for  $A_m$ ,  $A_t$ ,  $l_{o,t}$ , and  $E_t$ , thus allowing for a solution of the  $k_{sp}$  constant. The following table summarizes the scaling coefficients and exponents, which were taken



from the allometric curves. It should be noted that the Gastrocnemius muscle was chosen (somewhat arbitrarily) to scale the muscle/tendon properties. The allometric equations and curves are labeled “G” in the figure below (see Fig. 11).

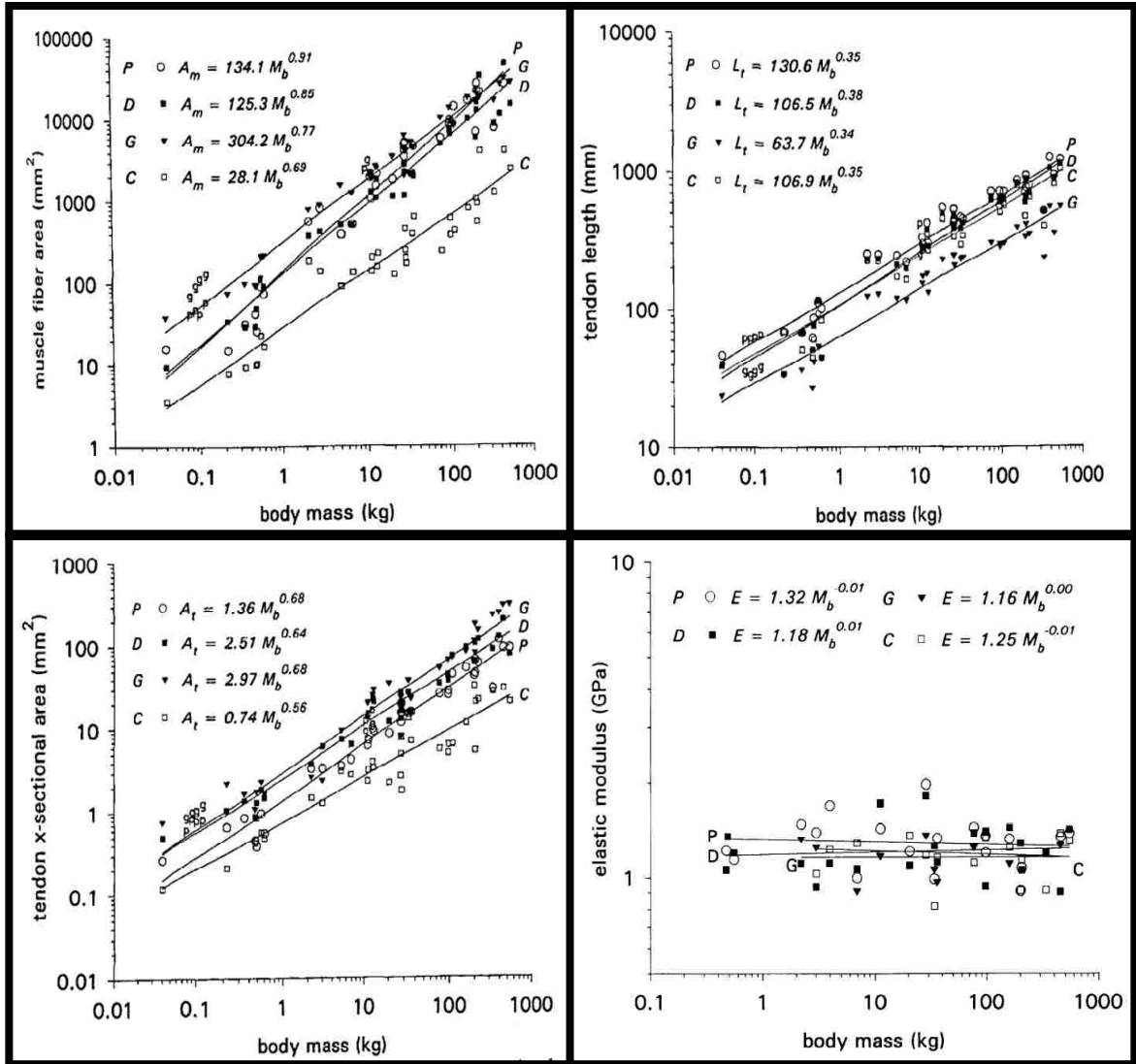


Figure 6: Allometric curves for scaling muscle-tendon properties (Pollock and Shadwick, 1994)

Once the biologically relevant spring constant was determined, multiple extension springs of different dimensions were gathered to include an appropriate range of stiffness for testing. A tension transducer (Futek) was fixed to a rigid mount on one end and the testing spring on its other end (see Fig. 12). The free end of the spring was attached to a variable load (0.85kg (30oz) or 1.3kg (45oz)) for testing. The mass was gently pulled downward at some arbitrary displacement. When the mass was released, the resulting oscillatory tension signal from the sensor was recorded in a Labview VI. The tension waveform was measured for its frequency and assumed to be equivalent to the system's natural frequency.

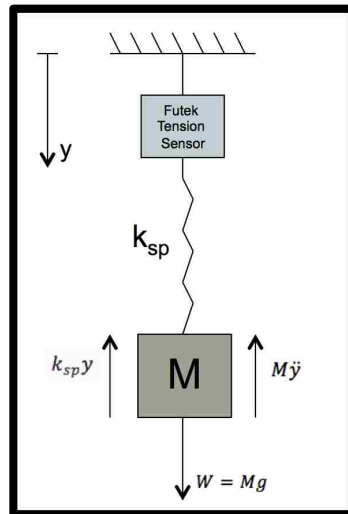


Figure 7: Oscillating spring-mass model for testing spring constants

The above figure (see Fig. 12) is a free body diagram of the experimental system for testing spring constants. It represents a simple model of the system, which relies on

the assumption that any damping is negligible in the system. The following equation of motion mathematically characterizes the system based on the free body diagram:

$$\ddot{y} + \left(\frac{k_{sp}}{M}\right)y = g$$

In the above equation,  $\ddot{y} \rightarrow$  the acceleration of the mass,  $k_{sp} \rightarrow$  the spring constant,  $M \rightarrow$  the mass of the load,  $y \rightarrow$  the displacement of the mass and  $g \rightarrow$  the gravitational constant  $\left(9.81 \frac{m}{s^2}\right)$ . Given the equation of motion listed above, the equation for system resonance frequency is given below.

$$\omega_n = \sqrt{\frac{k_{sp}}{M}}$$

Noting that:  $\omega_n = 2\pi f_n$

$$k_{sp} = M(2\pi f_n)^2$$

In the above equation,  $f_n \rightarrow$  the natural frequency of the system in Hz and  $\omega_n \rightarrow$  the natural frequency of the system in  $\frac{rad}{s}$ . By utilizing the equations, the springs could be characterized via their elastic coefficients. It should be noted that three trials were run for every spring and at each load in order to verify the accuracy of the results. The experiment was also conducted using the exact configuration of the AMTS's full tendon as assembled in the system. This was done in order to observe the contribution of spring elasticity to the system in relation to the contribution of elasticity in the filament and all of the connector pieces. Although these elements were assumed to be extremely rigid relative to the spring, this test was conducted to verify this assumption. The results of the

spring test are shown below (see Fig. 13) for the three springs that were chosen for application in the AMTS.

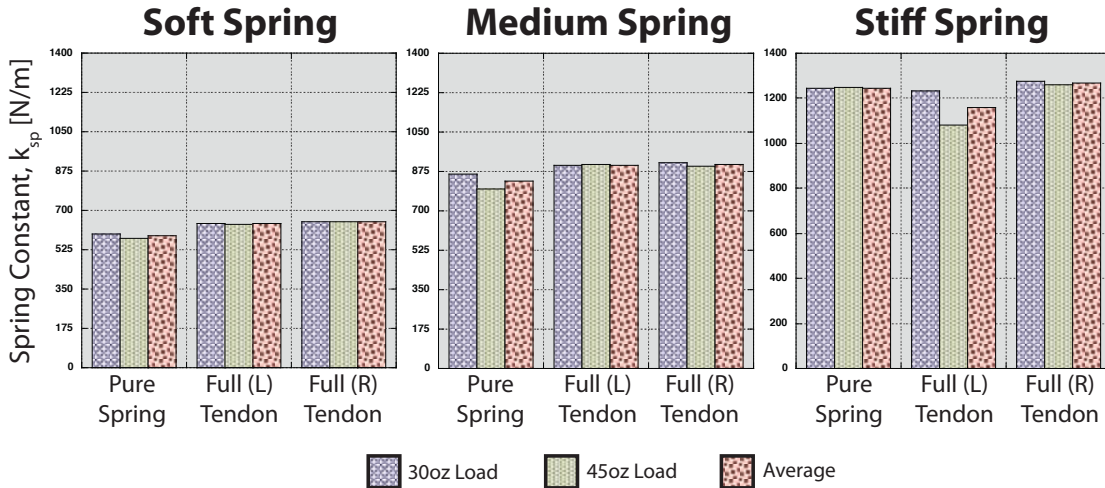


Figure 8: Spring constant test results

The bar graphs above show the results of the spring constant test. It should be noted that very little variance occurs in the data even for different loads tested. Also, the tendon elasticity tends to be slightly stiffer test for elasticity of just the spring. Finally, there is no statistical difference between the stiffness of the left tendon and the right tendon, even though its assembly is slightly different. The results of the selected springs via the spring constant test are summarized in the table below:

Table 5: Summary of spring constants

<b>Summary of Spring Constants</b>				
Spring Description	Associated C#	Symbol	Spring Constant [N/m]	Relative Spring Constant
<i>Soft</i>	C1	$k_{C1}$	640	$\sim 0.50 * k_{BIO}$
<i>Medium</i>	C2	$k_{C2}$	900	$\sim 0.75 * k_{BIO}$
<i>Stiff</i>	C3	$k_{C3}$	1200	$\sim 1.00 * k_{BIO}$
<i>Biologically Relevant</i>	.....	$k_{BIO}$	1190	.....

#### 2.4.2 Mass Moment of Inertia

The mass moment of inertia (MoI) for the system was determined by building a SolidWorks model of each rotating component and incorporating each component in a final assembly. In some cases, geometries were simplified slightly but the associated error in resulting mass MoI remains minimal. Also, the function that Solid Works utilizes in order to calculate these values was verified by comparing its values to theoretical values of simple geometries (e.g. a cylinder or tube). This verification process also ensured that the user was utilizing SolidWorks' function properly. Finally, all bolts were assumed to be point masses contributing to the mass MoI via the following equation:

$$J_{bolts} = \sum_{i=1}^{i=N_{bolts}} m_i * r_i^2$$

$$J_{fixed} = J_{Misc} + J_{bolts} + J_{LW}$$

In the above equations,  $J_{bolts}$  → the total mass MoI for all of the bolts in rotation,  $i$  → the respective bolt number,  $N_{bolts}$  → the total number of bolts rotating,  $m_i$  → the respective mass of bolt  $i$  (measured by an A&D Co. weight scale),  $r_i$  → the respective

distance between the point-mass representing the bolt and the axis of rotation,  $J_{fixed} \rightarrow$  the minimum mass MoI fixed in the system and  $J_{LW} \rightarrow$  the mass MoI of the load wheel.

The SolidWorks model is shown in the following images (See Fig. 14).



Figure 9: SolidWorks mass moment of inertia model

### 2.4.3 Damping Effects and Modeling the Passive System

In order to have a more robust understanding of the AMTS, a simple model of the passive part of the system (i.e. everything but the actuators) was deemed necessary.

Although elasticity had already been determined as well as the mass moment of inertia (refer to sections 2.4.1 and 2.4.2), any damping in the system had not yet been addressed. Thus, a simple model was constructed based off of the following block diagram (see Fig. 15).

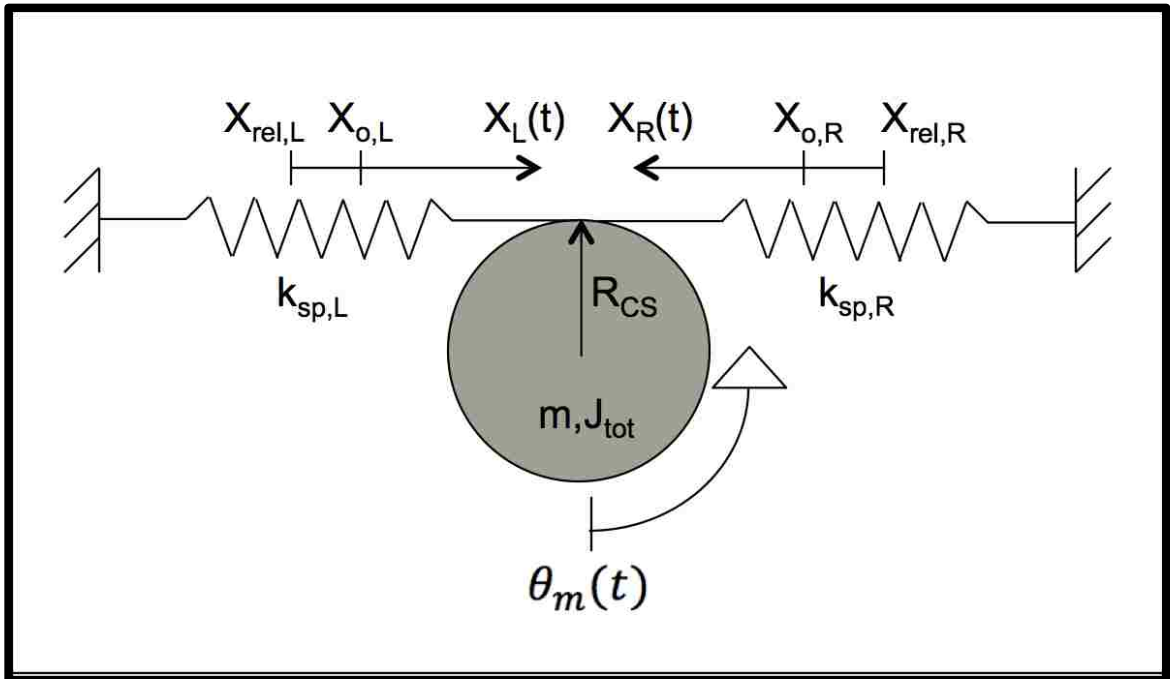


Figure 10: Model of the passive system

In the diagram (see Fig. 15) above,  $X_L(t) \rightarrow$  the linear reference frame of the left-side spring,  $X_R(t) \rightarrow$  the linear reference frame of the right-side spring,  $\theta_m(t) \rightarrow$  the reference frame for the center axis of rotation,  $R_{CS} \rightarrow$  the radius of the center spool (0.01m),  $k_{sp} \rightarrow$  the spring constant of the spring,  $m \rightarrow$  the total mass of all rigid bodies rotating,  $J_{tot} \rightarrow$  the total mass moment of inertia of all rigid bodies rotating,  $X_{rel} \rightarrow$  the end of the spring when it feels no tension,  $X_o \rightarrow$  the initial endpoint of the spring

assuming some pretension. The following diagram (see Fig. 16) shows a free body diagram of the passive system.

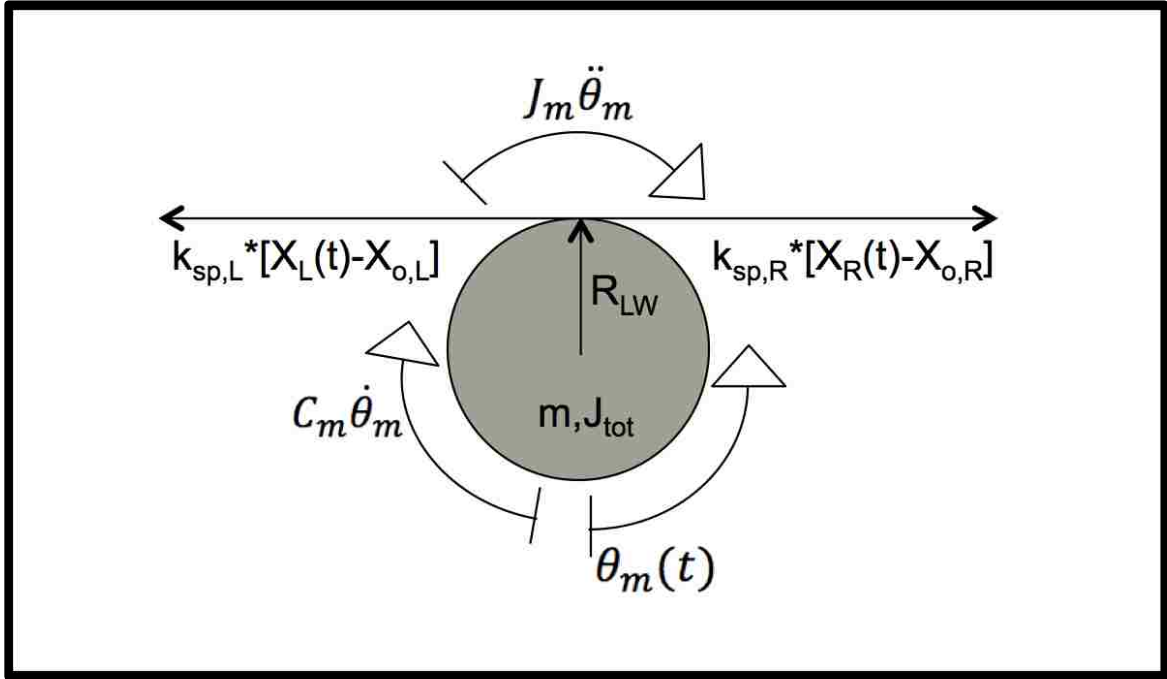


Figure 11: Free body diagram of the passive system

The following equations relate the two linear reference variables accounting for the motion of the springs to the rotational reference variable defining the motion of the wheel:

$$X_L(t) = -\theta_m(t)R_{CS}$$

$$X_R(t) = \theta_m(t)R_{CS}$$



By summing all moments about the center of the circle and making the appropriate substitutions referenced above, the following equation of motion is derived for the passive system:

$$-J_{tot}\ddot{\theta}_m - C_m\dot{\theta}_m - k_{sp,R}R_{CS}[\theta_m R_{CS} - X_{o,R}] + k_{sp,L}R_{CS}[-\theta_m R_{CS} - X_{o,L}] = 0$$

Noting that:  $k_{sp,L} = k_{sp,R} = k_{sp}$  and  $X_{o,L} = X_{o,R} = X_o$

The equation of motion is simplified:

$$J_{tot}\ddot{\theta}_m + C_m\dot{\theta}_m + 2k_{sp}R_{CS}^2\theta_m = 0$$

The equation displayed above describes the rotational motion of the system. It should be noted that it was assumed the line attached to the idle motors does not slip, and is therefore fixed. Also, it was assumed that all damping was viscous in nature (i.e. proportional to rotational velocity). In order to understand the natural frequency of the system, the following equation was derived from the equation of motion.

$$\omega_n = \sqrt{\frac{2k_{sp}R_{CS}^2}{J_{tot}}}$$

Also, the damped resonant frequency can be defined by the equation below.

$$\omega_{DR} = \omega_n\sqrt{1 - \xi^2}$$

In the above equations,  $\omega_n \rightarrow$  the natural frequency of the passive system,  $\omega_{DR} \rightarrow$  the damped resonant frequency of the passive system and  $\xi \rightarrow$  the damping ratio characterizing viscous damping in the passive system. By solving for  $\xi$ , the following expression is derived:

$$\xi = \left[ 1 - \left( \frac{\omega_{DR}}{\omega_n} \right)^2 \right]^{1/2}$$

In order to determine the damping ratio empirically, a simple experiment was conducted. While fully assembled and pre-tensioned, the load wheel was gently pulled on until it was displaced by some arbitrary angle. At the second the wheel was released, a stopwatch was initiated. At the maximum of every cycle, the stopwatch was pressed in order to measure the time period of the oscillations. Five trials were conducted for each of the three spring constants in order to verify that damping is constant in the system. Noting  $\omega_{DR} = \frac{2\pi}{\Delta t}$ , where  $\Delta t \rightarrow$  the average time period of the measured oscillation, the damping ratio was solved for a total of fifteen trials, five per spring constant. Per the experimental method just described, an average value of  $\xi = 0.3$  was determined for the damping ratio of the system. Ultimately, this value signifies a predominant oscillatory nature. Because  $\xi < 1$ , the system is under-damped. It should also be noted that the damping coefficient of the system is calculated by using the following mathematical definition of the damping ratio:

$$\xi = \frac{C_m}{C_c}$$

In the above equation,  $C_c \rightarrow$  the critical damping coefficient, which is given by the expression  $C_c = \sqrt{8k_{sp}R_{CS}^2J_{tot}}$ . Thus, solving the above equation for the damping coefficient and substituting the expression for the critical damping coefficient derives the following:

$$C_m = \xi \sqrt{8k_{sp}R_{CS}^2J_{tot}}$$

The table below (see Table 8) indicates the final damping coefficients that were solved.

**Table 6: Summary of damping coefficients**

<b>Summary of Damping Coefficients</b>				
$\xi$	#	$k_{sp}$ [N/M]	$J_{tot}$ [kg.m <sup>2</sup> ]	$C_m$ [Ns/m]
<b>0.3</b>	<b>1</b>	<b>645</b>	<b>0.02427</b>	<b>0.034</b>
<b><math>R_{CS}</math> [m]</b>	<b>2</b>	<b>905</b>	<b>0.03410</b>	<b>0.047</b>
<b>0.01</b>	<b>3</b>	<b>1213</b>	<b>0.04543</b>	<b>0.063</b>

#### **2.4.4 Tuning the Damped Resonant Frequency for Testing Purposes**

By successfully determining the damping ratio (refer to section 2.4.3), an important feat had been accomplished: a model for the passive system had been proven to conform to the physical system via resonance frequency testing. Thus, it was deemed practical to take advantage of the model for empirical bookkeeping. Specifically, a somewhat-arbitrary frequency was chosen for damped resonance,  $f_{DR}$ : 0.35Hz. Although there is no special significance to this frequency, it happens to be a convenient frequency for the system, in terms of its order of magnitude. As was discussed in Chapter 1 of this document, high torque oscillation frequencies are not terribly common in the biomechanics of mammalian locomotion. For example, if the AMTS were applied to a

prosthetic ankle, high oscillation frequencies would be an unnecessary requirement for this kind of an application.

Because the elastic coefficients of springs in the AMTS have always been of vital interest, it was determined that three different spring constants should be tested for in the system (the determination of these spring constants is described in section 2.4.1 of this document), at different frequencies relative to resonance. However, because resonant frequencies are proportional to the square root of the elastic coefficient, this means that testing for different springs would result in a new resonant frequency for each condition. In order to eliminate this consequence, it was decided that every testing spring should be coupled with a different mass moment of inertia (MoI) in order to maintain the resonant frequency at the previously agreed upon value of 0.35Hz.

Thus, a strategy for modulating the system's mass MoI was applied to the design of the actuator system. Utilizing a 3D-printed plastic (ABS) rail mounting system, 1.13kg (2.5lb) weights were placed on top of the load wheel at different radii away from the center of rotation. In this way, the flexibility of a variable radius allows for the system to feel the effects of the parallel axis theorem. This theorem is mathematically described below.

$$J_v = J_{cm} + md^2$$

In the above equation,  $J_v \rightarrow$  the variable MoI comprising of a displaced rigid body,  $J_{cm} \rightarrow$  the MoI for the rigid body when rotation occurs around its center of mass,  $m \rightarrow$  the mass of the rigid body and  $d \rightarrow$  the distance between the axis of rotation and the axis of rotation occurring about the center of mass of the rigid body. To summarize,

$d$  was modulated along with the spring constant in order to maintain the 0.35Hz resonant frequency of the passive system.

Specifically, the equation for resonant frequency utilized in determining the damping ratio (section 2.4.3) was applied as follows:

$$f_{DR} = \frac{\sqrt{1 - \xi^2}}{2\pi} * \sqrt{\frac{2R_{cs}^2 k_{sp}}{J_{tot}}}$$

Noting the following:  $J_{tot} = J_{fixed} + 2(J_{cm} + md^2)$

$$\text{Then, } f_{DR} = \frac{1}{2\pi} \sqrt{\frac{(2R_{cs}^2 k_{sp}) * (1 - \xi^2)}{J_{fixed} + 2(J_{cm} + md^2)}}$$

Finally, in order to determine the radius at which the added weights must be displaced,  $d$  is solved for in the following line:

$$d = \left[ \left( \frac{1}{2m} \right) * \left[ \left( \frac{(2R_{cs}^2 k_{sp}) * (1 - \xi^2)}{(2\pi f_{DR})^2} \right) - J_{fixed} - 2J_{cm} \right] \right]^{1/2}$$

In the above equations,  $f_{DR} \rightarrow$  the damped resonant frequency,  $\xi \rightarrow$  the damping ratio of the passive system (described in earlier sections of this document),  $R_{cs} \rightarrow$  the radius of the center spool (0.01m),  $k_{sp} \rightarrow$  the spring constant of choice,  $J_{fixed} \rightarrow$  the minimum mass MoI of the AMTS without any added weights,  $J_{cm} \rightarrow$  the mass MoI of the added weights rotating about their centers of mass,  $m \rightarrow$  the mass of the added weights ( $2.5lb \approx 0.45kg$ ) and  $d \rightarrow$  the distance between the axis of rotation about the center of mass of the added weights and the axis of rotation of the load wheel.

In application, an infinite degree of freedom with respect to the precision of variable radius  $d$  is not practical for accurate measurements. Thus, resonant frequencies were calculated as a function of  $d$  by varying its value in discrete and manageable measurement increments (e.g. 0.5cm). The resulting frequencies were very close to the 0.35Hz target and were all within a tolerance of less than 1% difference. The following table summarizes these results (see Table 9).

**Table 7: Summary of mass moment of inertia and resulting resonant frequencies**

		<b>Summary of Mass Mol and Resulting Resonant Frequencies</b>						
		#	$k_{sp}$ [N/m]	$d$ [m]	$J_{tot}$ [kg.m <sup>2</sup> ]	$f_{DR}$ Resulting [Hz]	$f_{DR}$ Desired [Hz]	Percent Diff. [%]
$J_{fixed}$ [kg.m <sup>2</sup> ]	6.64E-03	1	645	0.07	2.40E-02	0.352	0.35	0.57
$m$ [kg]	1.13	2	905	0.095	3.40E-02	0.350		0.09
$J_{cm}$ [kg.m <sup>2</sup> ]	3.41E-03	3	1213	0.115	4.50E-02	0.353		0.72

#### 2.4.5 Tuning Controller Gains

It is well understood that tuning a controller for a dynamic system is vital to the capacity of its function. However, what remains less clear is how to tune a given system. Regardless, there have been many different attempts to optimize this process. Much of this varying consideration can be attributed to the specific objective of the controller. For example, there are specific controllers meant to minimize or even eliminate overshoot in a system. This is called an over-damped system.

In the specific case of this artificial muscle-tendon system, a simple, classical approach has been taken. The PID controller has been implemented as a way of dealing with many of the transient unknowns in the system. Specifically, the piezoelectric motors introduce many unknown qualities that are inherently influential in the dynamics of the system. Although there have been mathematical models devised previously, which take these issues into account (Sun, 2010), they are extremely complicated and sensitive to the specific parameters of a given specific motor. This in conjunction with the inherent empirical nature of the project has led to the conclusion that developing such a model would be beyond the scope of this research.

Thus, a PID controller system was developed in order to deal with the various unpredictable behaviors of the system as a whole. In terms of tuning the various gains, a classical Zeigler-Nichols tuning (Ziegler and Nichols, 1942) was implemented in order to address the importance of perturbation rejection. Specifically, perturbation is an extremely important consideration for the controller, which is a result of dueling controllers running simultaneously, and blindly with respect to one another. The following equations describe the classical controller:

$$K_p = 0.6 * K_u$$

$$K_i = \frac{2 * K_p}{T_u}$$

$$K_d = \frac{K_p * T_u}{8}$$

In the above equation set,  $K_p \rightarrow$  the proportional gain,  $K_i \rightarrow$  the integral gain,  $K_d \rightarrow$  the derivative gain,  $K_u \rightarrow$  the minimum gain necessary to achieve oscillation around a set point when  $K_i = K_d = 0$  and  $T_u \rightarrow$  the time period of  $K_u$ 's oscillation.

Specifically, when one controller system reads feedback from the torque sensor (Futek), the other reads feedback from the tension sensor (Futek). In this way, the system is capable of providing a net torque at the load wheel while also regulating co-contraction in the antagonist motor. While this duel controller system is very effective at controlling for each individual objective, it can be tiresome for the system to deal with the two simultaneously. This is because every jump in the control signals for each controller acts as a perturbation to the other controller. In this way, each control system is constantly being challenged to reject perturbations from the opposite controller. For example, when the actuator starts at rest but begins to provide a net torque in a given direction, the constant co-contraction is perturbed by this tug coming from the other motor. Thus, it must deal with this sudden impulse as a perturbation. Similarly, the torque controller must deal with tugs on the line from the constant co-contraction controller as a relentless barrage of perturbation acting on the net torque of the load wheel. In order to deal with this constant volley of tugs between the agonist and antagonist motors, the Zeigler-Nichols tuning has been chosen to determine the proportional, integral and differentiator gains, or  $K_p$ ,  $K_i$  and  $K_d$  respectively.

In addition to the three gains of the PID controller system, a master gain was applied to each controller system,  $K_m$ . This master gain, when applied to the controller, scales up the proportionality of each gain relative to the next. This is necessary in order to compensate for the lack of an active model (i.e. a model including actuation) for the



system. The scaling of the master gain  $K_m$  was tuned empirically with the prime objective of minimizing error. Thus, in order to not bias the performance of the system in terms of the controller gains, the master gain for each individual parameter being tested was individually tuned by hand. The table below (see Table 10) lists all of the master gain values utilized in every trial.

Table 8: Summary of master gains used during experimentation

<b>Summary of Master Gains Used During Experimentation</b>						
	<b>Condition 1</b>					
	<b>Piezoelectric Motor</b>			<b>Electromagnetic Motor</b>		
<i>Frequency No.</i>	$K_{Tq}$	$K_{Tn}$ (Left)	$K_{Tn}$ (Right)	$K_{Tq}$	$K_{Tn}$ (Left)	$K_{Tn}$ (Right)
<i>f1</i>	2.500	0.020	0.015	2.000	0.060	0.060
<i>f2</i>	2.100	0.045	0.045	2.300	0.120	0.120
<i>f3</i>	2.500	0.080	0.050	2.700	0.150	0.150
<i>f4</i>	1.970	0.070	0.100	2.200	0.200	0.220
<i>f5</i>	2.570	0.094	0.110	1.900	0.220	0.150
<i>f6</i>	2.450	0.080	0.050	1.870	0.140	0.140
	<b>Condition 2</b>					
	<b>Piezoelectric Motor</b>			<b>Electromagnetic Motor</b>		
<i>Frequency No.</i>	$K_{Tq}$	$K_{Tn}$ (Left)	$K_{Tn}$ (Right)	$K_{Tq}$	$K_{Tn}$ (Left)	$K_{Tn}$ (Right)
<i>f1</i>	5.170	0.010	0.010	3.520	0.040	0.040
<i>f2</i>	4.760	0.030	0.030	3.730	0.050	0.050
<i>f3</i>	5.900	0.070	0.035	4.000	0.050	0.050
<i>f4</i>	5.150	0.070	0.060	4.900	0.043	0.043
<i>f5</i>	5.300	0.090	0.050	2.800	0.060	0.060
<i>f6</i>	5.200	0.100	0.080	2.500	0.080	0.080
	<b>Condition 3</b>					
	<b>Piezoelectric Motor</b>			<b>Electromagnetic Motor</b>		
<i>Frequency No.</i>	$K_{Tq}$	$K_{Tn}$ (Left)	$K_{Tn}$ (Right)	$K_{Tq}$	$K_{Tn}$ (Left)	$K_{Tn}$ (Right)
<i>f1</i>	2.800	0.005	0.008	2.000	0.033	0.033
<i>f2</i>	3.800	0.010	0.010	3.000	0.050	0.050
<i>f3</i>	4.600	0.025	0.015	3.470	0.050	0.050
<i>f4</i>	5.200	0.055	0.025	5.200	0.090	0.090
<i>f5</i>	5.100	0.055	0.040	5.500	0.050	0.050
<i>f6</i>	5.000	0.050	0.030	5.500	0.050	0.050

## **Chapter 3: Performance Evaluation of Actuators**

### **3.1 Actuator Comparisons**

#### **3.1.1 Electromagnetic Motors**

Electromagnetic Motors (EMs) have played a significant role in robotics research over the past several years. They are cheap, powerful, and provide a practical controller interface for most typical applications. Additionally, it is convenient that they scale up easily for higher or lower power applications. However, there are other design attributes that significantly limit the capacity of EMs to be more useful actuators, especially for biomimetic applications. Some of these limitations include the following: high velocity domain, reliance on bulky force transmissions (e.g. gear trains) for appropriate dynamic range, counter-electromotive force (CEMF), motor burnouts due to stalling, and etc...

One of the defining characteristics of electromagnetic motors remains their inherent propensity to spin at high rotational velocities. In some applications this is a positive attribute. For example, tattoo artists sometimes use a particular type of ink gun called a “rotary mechanism”. These machines basically utilize a crank-rocker mechanism where the output link is not fixed. Instead it is transformed from rotational motion to a linear motion at the tip by being guided into a closed funnel at its end. This allows the mechanism to output a small stroke of linear motion. In this application, an EM is ideal, because low force is required at very high velocities. However, this application is very much at odds with the kinds of needs that a locomotive robot or prosthetic limb might require. In other words, high rotational velocities must be transformed into a lower velocity domain in order to provide force-velocity properties appropriate for an artificial muscle.

Another problem with utilizing EMs for low velocity ranges is that of power capacity. For any motor, which has a linear force-velocity curve, a maximum power capacity can be found at  $0.5 \cdot n_{nl}$ , where  $n_{nl}$  is the rotational velocity of the motor with no load. However, because  $n_{nl}$  is typically very high, this means that the maximum power capacity of an EM tends to occur at very fast speeds. Thus, when utilizing an EM at low speeds, as would likely be necessary for biomimetic function, very little of the actuator's total power capacity is available. This effect can be seen in the following picture (see Fig. 1). It should be noted that this curve represents a general trend and is not representative of any specific data set. In other words, it is not to scale.

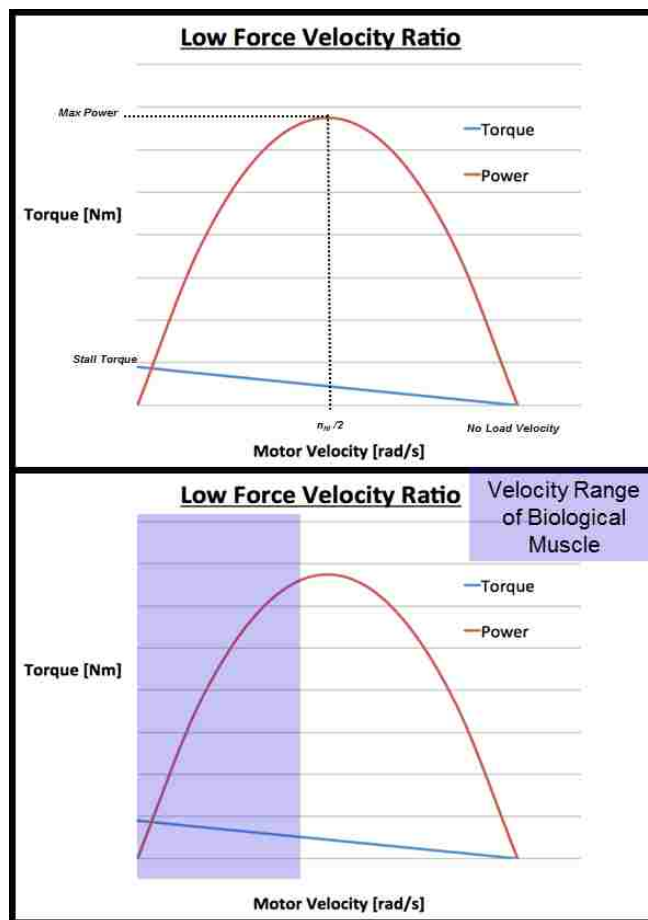


Figure 12: Low force-velocity ratio

In order to transform the force-velocity relationship indicative of electromagnetic motors, force transmissions such as gear trains are commonly used. Basically, by providing an interaction of the motor's rotor with a set of meshed gears, the system is capable of outputting a higher force/velocity ratio. While this is a common solution to the problem in robotics, there are many design disadvantages to gear trains, such as static frictional effects and efficiency losses. These unfavorable characteristics will be explored more thoroughly later in this section.

### 3.1.2 Piezoelectric Motors

Piezoelectric actuators represent a relatively new material innovation in actuator potential. However, there have been a number of designs developed over the past several years. Under the context of this project, ultrasonic rotary piezoelectric motors (PMs) have been selected based off of several design constraints. For an appropriate application to biomechanics a high torque-to-velocity relationship is required of its actuation. This parameter is based on the ratio of stall torque  $\tau_{stall}$  to no-load velocity  $n_{nl}$ , which tends to be fairly large in PMs relative to other actuator types. A generalized force-velocity curve is shown in the picture below (see Fig. 2). It should be noted that this curve represents a general trend and is not representative of any specific data set. In other words, it is not to scale.

Because piezoelectric motors exhibit a high force-velocity ratio, this also means that their peak power capacity occurs in a lower velocity range than that of electromagnetic motors. Thus, when utilizing PMs for actuation in biomechanical applications, a higher potential power capacity is available for consumption (see Fig. 2).

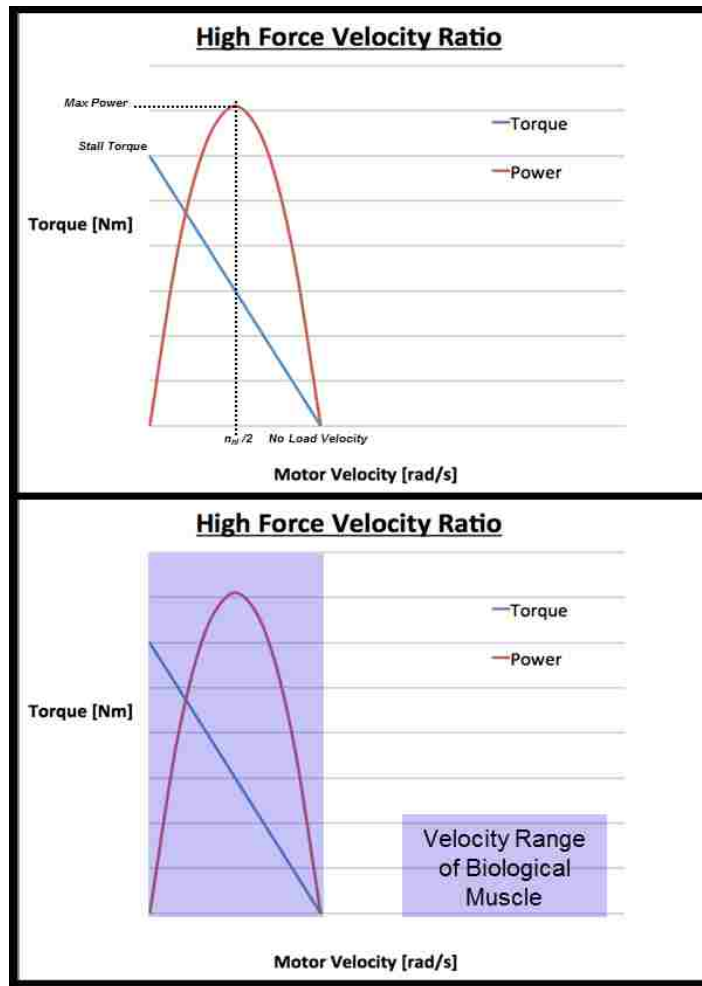


Figure 13: High force-velocity ratio

In order to transform the force-velocity relationship of an actuator, gearing is typically required. Electromagnetic motors (EMs) are a good example of this. As was iterated previously, EMs almost always require gearing, save for the smallest torque applications that rely on high speeds. Although gear drives could be applied to PMs for the opposite effect (i.e. speeding them up), it is perhaps more sensible to utilize particular actuators, which inherently exhibit a force-velocity relationship matched to the desired

output of a design. This rationale is justified by the dynamic limitations of gear drives in general.

Specifically, meshed spur gears are known to exhibit the following characteristics: (1) gear-windage losses, (2) static friction, or stiction (3) backlash and (4) mechanical failures due to stress concentrations. Windage effects describe the power consumption necessary to rotate the pinion and gear in the air-oil environment of a typical gearbox. Stiction refers to the static friction that gears must overcome at the interaction of their meshed teeth. Backlash exists in a non-ideal gear train where the teeth do not perfectly mesh. Basically, when small gaps exist between the teeth, there is always a lag when gears change direction and the gap must be made up before contact may be reestablished. This results in a small collision, which may cause vibration in the gear train.

All of these imperfections can comprise of a compounding detriment with mechanical consequences specific to the efficiency of its system. It has been shown empirically and theoretically that these effects can result in efficiencies anywhere between 98 and 99% per meshed coupling (Anderson and Loewenthal, 1980). Although these numbers may not sound high, the accumulation of multiple meshed-gear couplings can escalate losses rather quickly. For example, a 1000:1 micro metal gear motor from Pololu Robotics & Electronics contains seven meshed-gear couplings. Assuming an average efficiency of 98.5% per mesh, the gear train results in a total efficiency of slightly below 90%. This represents a significant amount of power loss in the system.

A fair alternative to gearing the output of a particular actuator is to choose one that already matches the ideal dynamics required of the system. Thus, for a biomechanical application, a high force-velocity ratio can be conveniently found in piezoelectric actuators. It should be noted that there is a fundamental feature found in both piezo-based actuators as well as biological muscle, which dominates their similar force-velocity characteristic. Ratcheting describes the basic operating principle, to which both actuators adhere.

In biological muscle, myosin heads are drawn toward the charged actin filament via a chemical bonding potential. As a muscle contracts, its myosin heads pull along the actin filament in synchronous manner. Thus, a bulk linear motion is dominated at the most fundamental level by this micro interaction. Similarly, piezoelectric motors utilize a small ratcheting mechanism of their own in order to output bulk motion. Specifically, ultrasonic rotary PMs maintain a ceramic-based core, which pulsates at a standing wave frequency of approximately 70~80Hz ([www.discovtech.com/](http://www.discovtech.com/)). As the piezoelectric core pulsates, stainless-steel blades called “pushers” are essentially wedged into the rotor. The pushers experience resonant vibrations at the ultrasonic resonances and elliptical displacements occur at their tips as a result. The elliptical pattern is designed to push the rotor along its inner surface such that bulk rotation occurs. The following images depict this interaction (see Fig. 3 and Fig. 4).



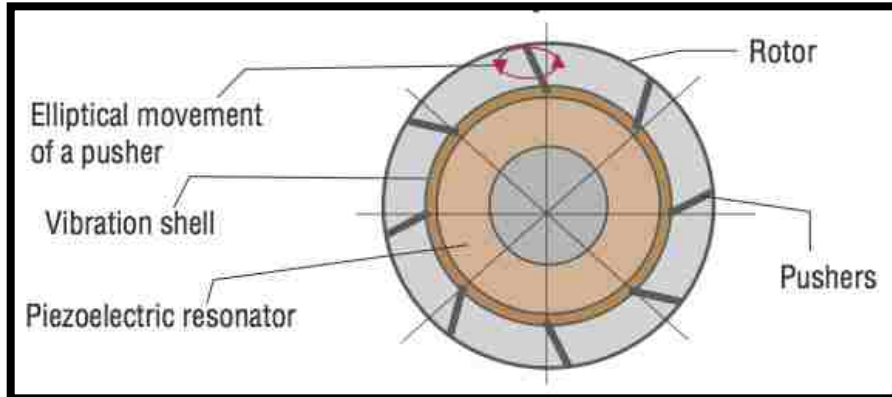


Figure 14: Cross-section of a piezoelectric motor

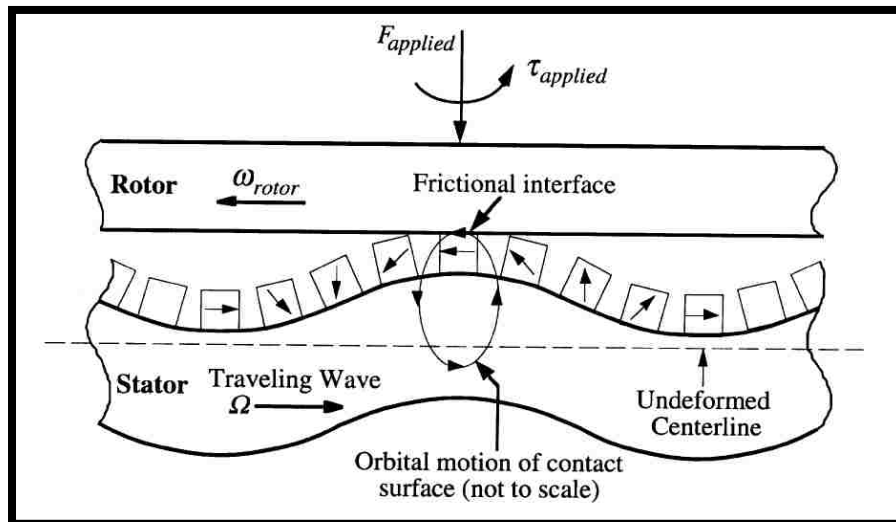


Figure 15: Piezoelectric motor diagram demonstrating a traveling wave

Although substantial models have been developed in order to predict some of the dynamic traits that ultrasonic rotary piezoelectric motors exhibit (Sun, 2002), they tend to be very complicated and extremely sensitive to appropriate input parameters of the model such as modeling of the ceramic materials in the lead zirconate titanate core of the motor. It should be noted that the research described in this document primarily emphasizes an empirical-based approach for actuator comparisons. Although the promise of modeling

cannot be denied, the basis of its process in this research is beyond the scope of experimental-based work in terms of the AMTS design and performance measurements.

There are many benefits of PMs that are unique to their specific design. One such attribute is its extremely high angular stepping resolution and accuracy. Specifically, a DTI PM-20R piezoelectric motor is capable of resolutions less than one arc-sec and an absolute accuracy of four arc-secs in its closed loop mode when using a high-resolution optical encoder (<http://www.discovtech.com/>). This particular trait is specifically made possible due to the small stroke of its ratcheting mechanism.

Another remarkable characteristic of PMs is that of an extremely fast response time (10-50 $\mu$ s). This ultra-fast sensitivity is due to a capacitive input impedance on the level of nano-farads as compared to the inductive input impedance of EMs on the level of milli-henries. PMs are also capable of being stalled safely and without a risk of the motor burning out. This is because a stall out turns out to be a simple mechanical jam at the steel pushers against the rotor. Similarly, when these actuators are not powered, they act as passive mechanical brakes, which require no additional electrical consumption.

Due to the incentive and unusual characteristics of piezoelectric motors, their conventional application in robotics has thus far been limited to high-resolution position controllers (e.g. an actuator for an electron microscope) and micro-actuators (Uchino, 1997; Flynn et al., 1992). However, piezoelectric motors have not yet been considered in larger biomechanical systems and specifically for the purposes of an artificial muscle. Thus, it is proposed that perhaps the superior position control of PMs can translate into more resolute force/torque control and fidelity as well. Specifically, the ratcheting

operating principle of PMs are considered for the specific application of biomechanical function in an artificial muscle tendon system.

### **3.1.3 Choice of Specific Actuators for Artificial Muscle**

Although the AMTS of current topic was designed with specific objectives in mind, it remains an effective testing platform flexible enough for evaluating a multitude of rotary motors. However, this study concerns itself with the specific comparison of electromagnetic motors to piezoelectric motors. Again, the context of a biomimetic application with respect to biomechanical function is vital to the testing backdrop of this study. Thus, these two motor types are incorporated into the design for the most relevant comparison.

The choice of electromagnetic motors for the study was made in order to represent a sort of “bread and butter” actuator type within robotics industry today. However, the concept of utilizing piezoelectric motors for force feedback in biomechanical robotics is a somewhat novel idea. Thus, the intent is to compare the respective motor performance of a typical actuator with a non-typical actuator.

Specifically, the models representing both motor types were chosen by a couple of key manufacturing specifications. In order to match the inherent dynamics in both actuators, stall torques and no-load speeds were specifically compared. Also, weight and current draw were considered. These considerations helped result in the particular actuator choices summarized in the following table (see Table 2).

Table 9: Motor specifications table

<b>Motor Specifications Table</b>				
<b>Motor Type</b>			Piezoelectric	Electromagnetic
<b>Company</b>			DTI	Pololu
<b>Model</b>			PM-20R	Micro Metal Gearmotor
<b>Specification Type</b>	<b>Symbol</b>	<b>Units</b>	<b>Value</b>	
No Load Speed	$n_{nl}$	rad/s	5.24	1.47
Stall Torque	$T_{stall}$	Nm	0.11	0.49
Voltage Supply	$V_{sup}$	V	12	6
Stall Current	$I_{stall}$	mA	400	360
Gear Ratio	G.R.	#	1:1 (Direct Drive)	986:1
Weight	W	kg	0.1	0.011

It should be noted that the no-load speed of the particular electromagnetic motor chosen is in fact slower than that of the piezoelectric counterpart. Although this specification may seem at ends with the concept that electromagnetic actuators tend to have a low force-velocity ratio, it is recalled that this conclusion considers a pure motor output, before any gearing or transmission. Thus, it should be pointed out that the electromagnetic motors are only capable of exhibiting such low speeds with its 986:1 gearing ratio. In reality, the actuator's implicit no-load velocity is approximately three orders of magnitude faster.

The following are example images of the two motor types (See Fig. 6).

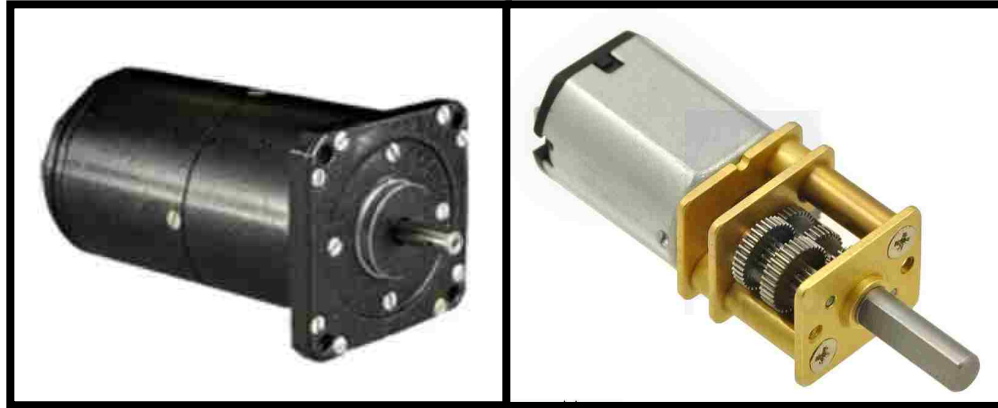


Figure 16: Piezoelectric motor choice (left) and geared DC motor (right)

Table 10: Auxiliary hardware

<b>Auxiliary Hardware</b>					
#	Hardware	Company	Model	Voltage	Current
1	EM Power Supply	Agilent	E3630A DC Supply	0-6V	2.5A
2	EM Motor Driver	Pololu	MD03A H-Bridge	.....	.....
3	PM Power Supply	BK Precision	1760A DC Supply	0-30V	2.0A
4	Connector Block	NI	SCB-68	.....	.....
5	Counter-Timer Card	NI	PICe-6320	.....	.....

## 3.2 Testing Protocol, Results and Discussion

### 3.2.1 Methods

The identification of some quality or measurement with respect to the understanding of a physical nature desired is extremely vital to the organization of experimental design. In other words, in order to understand a path forward, one must identify an end goal. Of course, paths are not always readily available or clear from the outset, especially in research and science. However, the clarity of an objective can oftentimes bleed precedence into the clarity of a trajectory. Simply put, planning helps

organize the process. Thus, a few key parameters were identified early on such that an appropriate experimental design could be outlined for this particular research.

Specifically, error  $E$  has been earmarked as an important measure of fidelity with respect to the controller signals of both control schemes (i.e. net torque and opposing tension). Additionally, another key parameter was identified for empirical monitoring: system efficiency,  $\eta$ . In less formal terms, these two parameters (i.e. error and efficiency) were chosen in order to shed light on the performance of EMs and PMs relative to one another and in the context of a biomimetic AMTS. Thus, an appropriate experimental design was developed under the constraints of measuring the necessary parameters for error and efficiency.

Given that the control subsystems of the AMTS already rely on error between the target torque/tension profile and the instantaneous measurement(s) of torque/tension that the system is physically experiencing, this was an easy parameter to measure for data analysis. Simply put, the instantaneous error for both torque control and tension control was saved with each iteration of the controller frequency (i.e. 50Hz), per trial. However, in order to run a single experimental trial, there was a thorough preparation process. This process will be described in the paragraphs and organizational table (see Table 11) following immediately below.

The first step in an experimental trial run typical to this study involves the identification of the following parameters: motor type (e.g. EM or PM), condition number (e.g. C1 → C3), frequency number (e.g. f1 → f6), and trial number (e.g. 01 → 03). The motor type refers to the motors being tested in the particular trial. The condition

number refers to a whole suite of parameter settings, which are all dependent on each other. The frequency number refers to the prescribed frequency of the controller sine waveform. Finally, the trial number refers to how many times the particular combination of parameters has been run. The following table summarizes the different parameters combinations that were tested (see Table 11).

**Table 11: Testing parameter combinations**

<b>Testing Parameter Combinations</b>								
Parameter Label	Sub-Parameter Label	Parameter Values						No. of Trials
<i>Motor</i>	<i>Motor Type</i>	PM	EM					2
<i>Condition</i>	<i>Condition Number</i>	C1	C2	C3				3
	<i>Spring Constant, <math>k_{sp}</math> [N/m]</i>	640	900	1200				
	<i>Prescribed Torque Magnitude [Nm]</i>	0.0190	0.0267	0.0320				
	<i>Mass Mol, <math>J</math> [kg.m<sup>2</sup>]</i>	0.0243	0.0341	0.0454				
	<i>Tension, <math>T_c</math> [N]</i>	0.9500	1.3400	1.7800				
<i>Prescribed Frequency</i>	<i>Frequency Number</i>	1	2	3	4	5	6	6
	<i>Relative Frequency, <math>f/f_{DR}</math> [#]</i>	0.5	1.0	1.5	2.0	2.5	3.0	
	<i>Absolute Frequency, <math>f</math> [Hz]</i>	0.175	0.350	0.525	0.700	0.875	1.050	
<i>Trial</i>	<i>Trial Number</i>	01	02	03				3
<i>Total Number of Trials</i>							<b>108</b>	

It should be noted that the all of the values associated with the condition number parameters were determined as a linear function of the spring constant in condition number three. This means that since the spring constant in condition number two is approximately three-fourths of this value in condition number three, then the prescribed torque magnitude, the mass moment of inertia and the co-contraction tension of condition number two are all approximately equal to three-fourths of the value of their respective counterparts in condition number three. Thus, the proportionality of all of these parameters was kept constant for each condition number. In this way, the experimental

design allowed for different spring constants to be tested independently of competing parameter changes, the hope being to isolate any unintended parameter change effects in the performance of the actuator system.

Another point worth mentioning is the selection of specific prescribed frequencies for testing. First, all frequencies were chosen relative to the damped resonant frequency ( $f_{DR} = 0.35\text{Hz}$ ) of the system. Because it is physically impossible to test every range of frequencies relative to the damped resonant frequency, the span of a single order of magnitude was chosen and partitioned into six discrete frequencies increasing by  $0.5*f_{DR}$  each time. The following range approximates this order of magnitude:  $0.1 \rightarrow 1.0\text{Hz}$ . This range was decided upon because it is the order of magnitude containing the damped resonant value as well as a relevant range of biomimetic frequencies. Although biological muscle-tendon systems are not absolutely restricted to this range of oscillation frequencies, it is capable of characterizing most typical function.

Once all of the parameters were identified, the Labview virtual instrument (VI) executed its code. The power supply was turned on as well as the DAQ system. Next, all transducers were nulled via a custom built Labview function where all data was averaged over a five-second time period. The resulting mean values were stored in the program and subtracted out from the measured signals throughout the rest of the trial. In order for the tension transducers (Futek) to be nulled, they were disconnected from the line and hung free of any tension in order to get an accurate null value. Similarly, no motion was instigated about the torque transducer (Futek) so that an accurate null value could be found. No signal was sent to the motors such that an accurate null value could be found for the current running through the shunt resistors.



After the null values were calculated, the tension transducers (Futek) were reconnected in series with the springs. Next, the Labview code executed a while loop in order to pre-tension the tendons to the appropriate tension equivalent to the set point of a given trial. In this way, the trial would begin with no error (ideally). As the AMTS was pre-tensioned, the load wheel was rotated until both springs were approximately equidistant from the axis of rotation. This centering task would help ensure that a sensor or spring never got wrapped around the center tube support. If it did, this trial was thrown out and not recorded.

Finally, with the system pre-tensioned and centered, the Labview code would begin a standby phase of the trial. This means that actuator system attempts to provide net torque at the load wheel even though no data is being collected yet. During this stage, all final master controller gains were fine-tuned and the device was given a few cycles to reach a steady-state operation. Also, a Miro camera (Vision Research) was set to capture video of the tension transducer's displacement as a function of time such that eventually this could be used to help calculate mechanical power output via the output velocity of the system. All of the camera settings are organized in the table below (See Table 12).

**Table 12: Miro camera settings**

<b>Miro Camera Settings</b>				
<b>#</b>	<b>Setting</b>	<b>Symbol</b>	<b>Value</b>	<b>Unit</b>
<b>1</b>	<b>Resolution</b>	res	640x480	Pixels <sup>2</sup>
<b>2</b>	<b>Frame Rate Frequency</b>	$f_{cam}$	50	Hz
<b>3</b>	<b>Exposure Time</b>	$t_{exp}$	2000	$\mu s$
<b>4</b>	<b>Camera Distance</b>	dist	~3	m

Once the steady-state operation of the AMTS was reached, a record function coded into Labview was indicated such that data collection would begin at approximately the beginning of the next cycle. The record function would collect data for five full cycles and continue on for a sixth cycle such that no braking effects would alter the data during the last cycle. After the last cycle was completed, a post-trigger digital signal was sent to the Miro camera in order to stop filming and synchronize the data. The video frames associated with the trial were saved by indicating the total number of frames recorded. This calculation is provided in the line below:

$$\text{Total No. of Frames Recorded} = \left(\frac{1}{f}\right) * N_{cycles} * f_{cam}$$

In the above equation,  $f \rightarrow$  the input frequency of the prescribed torque target,  $N_{cycles} \rightarrow$  the number of cycles recorded (5) and  $f_{cam} \rightarrow$  the frame rate of the camera (50Hz).

This being a typical trial run, three trials were conducted for a total of fifteen complete cycles for each of the thirty-six parameter combinations resulting in a total of one hundred and eight trials for the study. For every one of the one hundred and eight trials, two different error profiles were recorded: one for torque error and one for tension error. After all of the torque errors were recorded and saved, they were read in a separate Labview VI. When executed, the VI prompts the user to choose which files to read. After the appropriate file for the desired trial is picked, the VI takes both error profiles and sums the absolute value of the individual elements in each error array in order to have a total sum of error for every cycle in a particular trial. This summed error is then divided by the number of data points in the cycle. This produces an average amount of error

magnitude per data point. Once these values were calculated for all fifteen cycles in three trials for the particular set of parameters, a final average was found for the error magnitude per data point. Finally, these errors were normalized to the magnitude of the prescribed torque profile for torque error and the magnitude of co-contraction for the tension error. The following equation mathematically describes the error-calculating algorithm, which was just explained.

$$\text{Summation of Error} = \sum_{j=1}^{j=N_{dp}} (\text{Tar.} - \text{Act.})$$

$$\text{Ave. Error per Cycle} = \frac{\text{Summation of Error}}{N_{cycles}}$$

$$\text{Ave. Error per Data Point} = \text{Ave. Error per Cycle} * \left( \frac{f}{f_{ctrl}} \right)$$

In the equation set above,  $N_{dp}$  → the number of data points in a given trial, **Tar.** → the target torque/tension prescribed for the trial, **Act.** → the instantaneous measurement of torque/tension that the system is experiencing,  $N_{cycles}$  → the number of cycles per trial (5),  $f$  → the prescribed torque frequency for the trial,  $f_{ctrl}$  → the controller frequency (50Hz).

Error for both torque and tension was tabulated for every condition and frequency tested. Finally, all of these data were plotted for comparison. It should be noted that these results are shown and discussed in section 3.2.2 of this document.

It should be noted that the same set of the trials used to measure error were also used to measure system efficiency. However, different methods and measurements were

taken. Generally speaking, efficiency is always a ratio of a system's energy output to its energy input. In the case of this AMTS, the output is defined as the mechanical energy of the load wheel rotating and the input is its electrical energy consumption. This equation can be found below.

$$Efficiency = 100\% * \left( \frac{Mechanical\ Energy\ Output}{Electrical\ Energy\ Consumption} \right)$$

In order to calculate electrical energy consumption, voltage and current were measured with National Instruments DAQ card, PCI-6251. Specifically, a shunt resistor was placed in series with each motor driver and the motor being driven. Thus, using Ohm's Law, the voltage differential measured over the shunt resistor could be divided by its resistance in order to get the current in the circuit. Ohm's Law is solved for current in the equation below.

$$I = \frac{V_{shunt}}{R_{shunt}}$$

In the above equation,  $V_{shunt} \rightarrow$  the voltage differential measured over the shunt resistor,  $R_{shunt} \rightarrow$  the resistance of the shunt resistor and  $I \rightarrow$  the current in the circuit.

For practical purposes, this shunt resistor was placed after the motor driver circuit but before the motor in the case of the electromagnetic motors and before both the driver circuit and the motor in the case of the piezoelectric motors. Thus, the total voltage feeding current to the PMs was always the programmed value of the power supply, or  $V_{PM} = 12V$ . However, because the shunt resistor was placed after the circuit in the case of the EMs, the voltage was expressed in terms of the circuit's current (which is

conserved since the resistor is in series with the motor) and the motor's resistance via the following equation.

$$V_{EM} = \frac{I_{EM}}{R_{EM}}$$

In the above equation,  $V_{EM}$  → the voltage of the electromagnetic motor,  $I_{EM}$  → the current in the circuit of the electromagnetic motor and  $R_{EM}$  → the resistance of the motor (measured by an ohmmeter to be 15.5Ω). In order to calculate instantaneous electrical power consumption by the motors, the following equation was used.

$$P_{elec} = V * I$$

In the above equation,  $P_{elec}$  → electrical power consumption,  $V$  → voltage and  $I$  → current. It should be noted that the power eaten up by the shunt resistors themselves was not considered. This is because the voltage measurements were nulled while the loads of the resistors were being powered. Another important point of discussion lies in the selection process of the shunt resistors. There were two opposing design constraints, which were considered when choosing these resistances. The first constraint observes the fact that Ohm Law predicts a larger voltage differential at the resistor when its resistance is higher. This is because voltage is proportional to resistance. Thus, a large enough resistance was deemed necessary in order to get a signal with an acceptable signal-to-noise ratio. At the same time, the larger the resistor is, the more power dissipation occurs, leading to a decrease in efficiency. Thus, it was also deemed that the resistance of the shunt resistor should only be as large as it had to be.

To address this issue, a very small resistor was tested for voltage signals in the condition with the lowest expected current draw (condition number C1 at frequency 0.175Hz). The resistance of the shunt resistor was slowly increased until a legible signal could be read. This method resulted in a shunt resistor of  $10\Omega$  for the case of the piezoelectric motors, and a resistance of  $0.47\Omega$  for the electromagnetic motors. Although it may seem that the shunt resistor of the piezoelectric motors may have resulted in more power dissipation due to a higher amount of resistance added to the circuit, this is not necessarily true. In actuality, it is the relative resistance of the shunt resistor to the total resistance of the entire circuit, which dictates what percentage of power dissipation occurs at the shunt resistor. Thus, due to the fact that the piezoelectric materials generally have a much higher resistance than the armature of an electromagnetic motor, the discrepancy is to be expected.

For all trials, electrical power consumption of each motor was recorded and saved. The power consumption for each motor was then summed together to give the total electrical power consumption over time. Once all trials were completed, the total electrical power consumption profile was integrated over the time of the five completed cycles in order to calculate the amount of electrical energy consumption for the full trial. This value was then divided by the number of cycles in the trial (5) in order to get an average value of energy consumption per cycle. The following equations describe the mathematical process explained just above.

$$E_{elec} = \int [P_{elec,L} + P_{elec,R}] dt$$

$$Ave. E_{elec} = \frac{E_{elec}}{N_{cycles}}$$

At the same time that electrical power consumption was being recorded during the trials, mechanical output power was being monitored via the velocity of the lines feeding the load wheel's axis of rotation as well as the tension in the lines. Specifically, a Miro camera from Vision Research was used in conjunction with Phantom Camera Control (PCC v2.5) image capture software and a marker tracking function built for MATLAB by Ty Hedrick of the University of North Carolina at Chapel Hill (Hedrick, 2008).

Although the output power of the AMTS can clearly be defined by the force and velocity of the load wheel, these parameters could not give any insight on the efficiency of individual motors (e.g. left or right side). Thus, assuming that the tendon lines never go slack (i.e. tension = 0 N), the rotational velocity of the wheel must be proportional to the linear velocity of the lines pulling on the center support tube. This linear relationship is given by the following equation:

$$\omega_{LW} = \frac{v_{lin}}{R_{cs}}$$

In the above equation,  $\omega_{LW} \rightarrow$  the rotational velocity of the load wheel,  $v_{lin} \rightarrow$  the linear velocity of the line wrapping around the center spool and  $R_{cs} \rightarrow$  the radius of the center support tube (0.01m). Similarly, the torque magnitude felt at the load wheel must also be proportional to the tension felt in the line minus the opposing pretension. This linear relationship is shown in the equation below.

$$T_{\tau} = T_{tot} - T_{cc} = \frac{\tau_{LW}}{R_{cs}}$$

In the above equation,  $T_{\tau}$  → the tension driving net torque at the load wheel,  $T_{tot}$  → the total tension in the line,  $T_{cc}$  → the co-contractive tension in the line opposing net torque,  $\tau_{LW}$  → the torque felt by the load wheel and  $R_{cs}$  → the radius of the center spool (0.01m). It is also noted that mechanical power may be defined by the following equation:

$$P_{mech} = \vec{F} \cdot \vec{v}$$

Thus, assuming that the line is approximately horizontal (i.e. the tension force vector is oriented in the same direction as the horizontal component of the velocity vector)...

$$P_{mech} = T_{\tau} * v_{lin,x}$$

In the above equations,  $P_{mech}$  → the mechanical power output of the system,  $\vec{F}$  → force vector,  $\vec{v}$  → velocity vector, and  $T_{\tau}$  and  $v_{lin,x}$  are defined in earlier equations. It should be noted that in reality there were very small amounts of power dissipation at the rotating joint in between the tension lines and the load wheel. However, these losses were assumed to be small enough to neglect, given that ball bearings typically result in minimal losses relative to the total magnitude of power in the system.

Because the total tension in the lines was already recorded for tension error calculations, the other measurement needed for mechanical power output was the output velocity in the lines. Thus, the inline tension transducers (Futek) were chosen as rigid



bodies to mark for tracking with the MATLAB function. In order to optimize the tracking function, a white sticker with a black ink dot was stuck to the center of each tension transducer before the trials were recorded. This enabled easy tracking performance via contrast in the MATLAB function. Also, two black ink dots were marked on the support frame of the AMTS at 0.035m apart. Because these two dots never saw any displacement throughout the trial, their average pixel displacement could serve as an accurate displacement calibration for the tracking of the tension transducers. Below is an example of the tracking function in MATLAB during an arbitrarily picked trial.

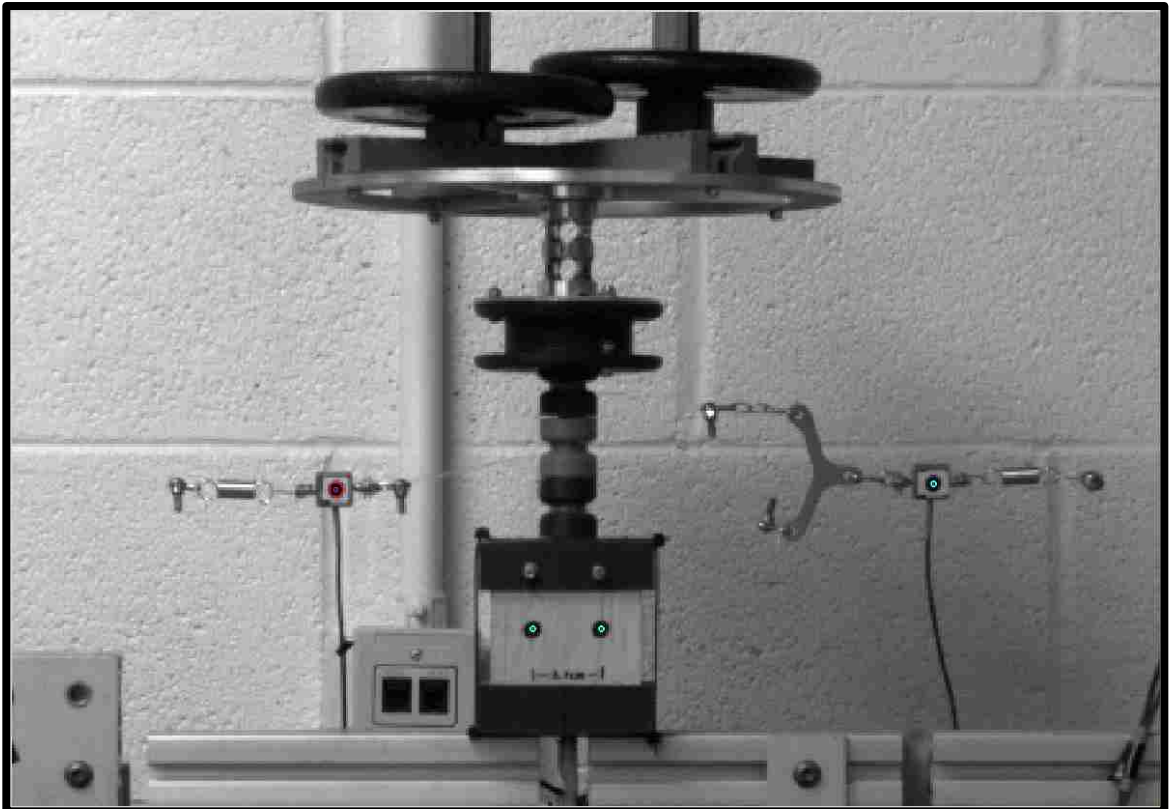


Figure 17: Matlab tracking function example

After the MATLAB function performed its displacement tracking on the tension transducers, the horizontal component of the displacement vectors were read in the Labview VI for calculating mechanical power output. First, the horizontal displacements were all multiplied by the conversion factor determined by the calibration dots:

$\left(\frac{0.035m}{27\ pixels}\right)$ . Next, both displacement arrays were differentiated with a built-in Labview function using the “backwards” method. This produced horizontal velocity arrays for both tension transducers as a function of time. Finally, mechanical power output was calculated via the equations listed previous.

Mechanical energy output was calculated by integrating the power curves over the total time of the trial run. The mechanical energy output for each motor was added together and then divided by the total number of cycles (5) to get an average total mechanical energy output per cycle.

$$E_{mech} = \int [P_{mech,L} + P_{mech,R}] dt$$

$$Ave. E_{mech} = \frac{E_{mech}}{N_{cycles}}$$

Finally, the total average efficiency of the AMTS was calculated by dividing the average mechanical energy per cycle by the average electrical energy consumption per cycle. All three trials for the same parameters were averaged to get a final value for efficiency at the particular conditions and frequency of the trial.

### 3.2.2 Results: Overview

One of the largest challenges to this study became the push to find relevance in mountains of data. Although the prospect of an artificial muscle sharing fundamental operating principles with biological muscle (i.e. ratcheting mechanism) seems promising, it was always unknown in exactly what way the piezoelectric motors (PM) would reveal their true colors in contrast to the capability of electromagnetic motors (EM) as an example of abstract actuator technology seemingly so at ends with biology. Thusly, multiple parameter combinations were decided upon as part of an aggressive strategy aiming to tease apart the potentially subtle differences between PMs and EMs.

This section will focus on showcasing the entirety of this study's results in a broad sense. The subsequent sections following will attempt to compress and reorganize the most insightful pieces of data into the most useful combinations while simultaneously noting useful takeaways. The plots on the following page (see Fig. 18) lay out an inclusive formatting of all the data collected during this study. It should be noted that every column of plots on the left is data collected from the PMs while every plot in the right column is that of the EMs. Also, each row of plots signifies a different parameter, which was measured. These include: normalized torque error  $\left(\frac{E_{Tq}}{\tau_{max}}\right)$ , normalized tension error  $\left(\frac{E_{Tn}}{T_{cc}}\right)$  and efficiency  $\eta$ .

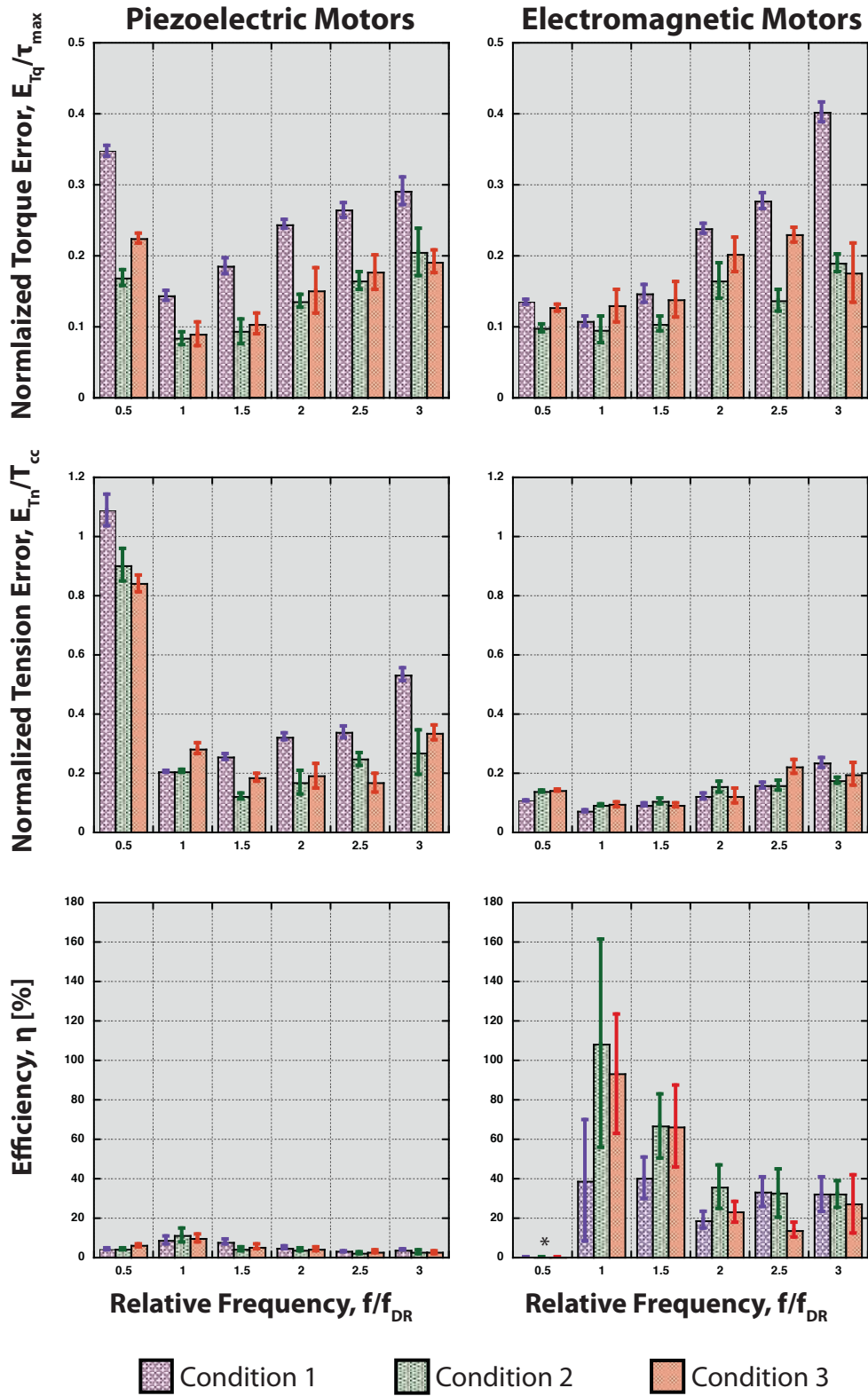


Figure 18: All-inclusive data results

Some of the more apparent observations in the above dataset are signified by the following relative frequency:  $f_{rel} = 1$ . This value, of course, refers to the frequency that signifies when the system is excited at resonance. As such, two general trends can be picked out. Firstly, a minimum of error tends to occur at this frequency. In particular, this trend may be viewed in the normalized torque error data. Furthermore, this global minimum tends to show itself more pronounced under conditions that are more prone to error (e.g. Condition 1) as an exaggeration.

In the normalized tension error data, this trend of minimal error at resonance is much less distinctive. However, this is not surprising. In the case of torque control, the system is attempting a sinusoidal waveform of torque set points. This is very different from the step input of constant tension, which is simultaneously controlled for in the co-contracting antagonist. Because a step input is not a repeatable, periodic function, its error as a manifestation of the tension controller is much less sensitive to resonance in the system. However, a slightly different trend can be noticed in the data.

Primarily, a slow but appreciable rise in error occurs in the higher end of the frequency domain. This result is sensible given that a constant co-contracting tension is intuitively harder to control as higher torque magnitudes are oscillated between opposing directions in smaller time periods. In other words, the higher end of the frequency domain represents a more volatile control space, ultimately resulting in more of a jerky action. This rise in error can also be seen in the torque control as the input frequency increases.

It may be observed that the piezoelectric motors perform badly in particular at the frequency at half of resonance. This trend is interpreted to be a result of an extremely

high response actuator (10-50 $\mu$ s) attempting to control for very slow input frequencies at a controller frequency three orders of magnitude smaller (50Hz  $\rightarrow$  20ms). This controller frequency is very comparable with the response time of a typical electromagnetic motor (~10ms). Thus, an unfair advantage may exist for the electromagnetic motor under the particular design constraints of a 50Hz controller frequency. This phenomenon will be discussed in more detail in the final section of this chapter (3.2.4).

Following this rationale for explaining a general lackluster performance on the part of the piezoelectric motors, the efficiency data are perhaps the most telling of this result. It is interesting to note that an inverse relationship between error and efficiency can be seen for both motors and in all condition numbers. This is to say that as error minimizes at resonance, system efficiency peaks. This is a logical and rational outcome, which helps lend credence to the study at hand. Regardless, there is a clear shift in the data of the piezoelectric motors as compared to the data of the electromagnetic motors. While the former hovers at efficiency levels near around 10%, the latter ranges from approximately 30-100%.

It should also be noted that no data from the slowest frequency was included for the electromagnetic motors (\*). All data that were collected at this frequency were deemed an anomaly due to artificially low power consumptive values resulting from a current signal to low to accurately measure. Thus, efficiencies were artificially robust to the point of a non-sensible result. Nonetheless, very high efficiencies like the results seen for the electromagnetic motor at resonance are in part explained by the potential energy interactions as an influence of the extension springs at resonance.

### 3.2.3 Condition Number Trends

In order to gain a clearer view on the data, specifically in terms of the varying condition number, this section will attempt to reorganize it by negating the trends dependent of frequency. In other words, the mean value across the frequency domain was calculated for both motors at all three conditions for normalized torque error. The following plot communicates these results (see Fig. 19).

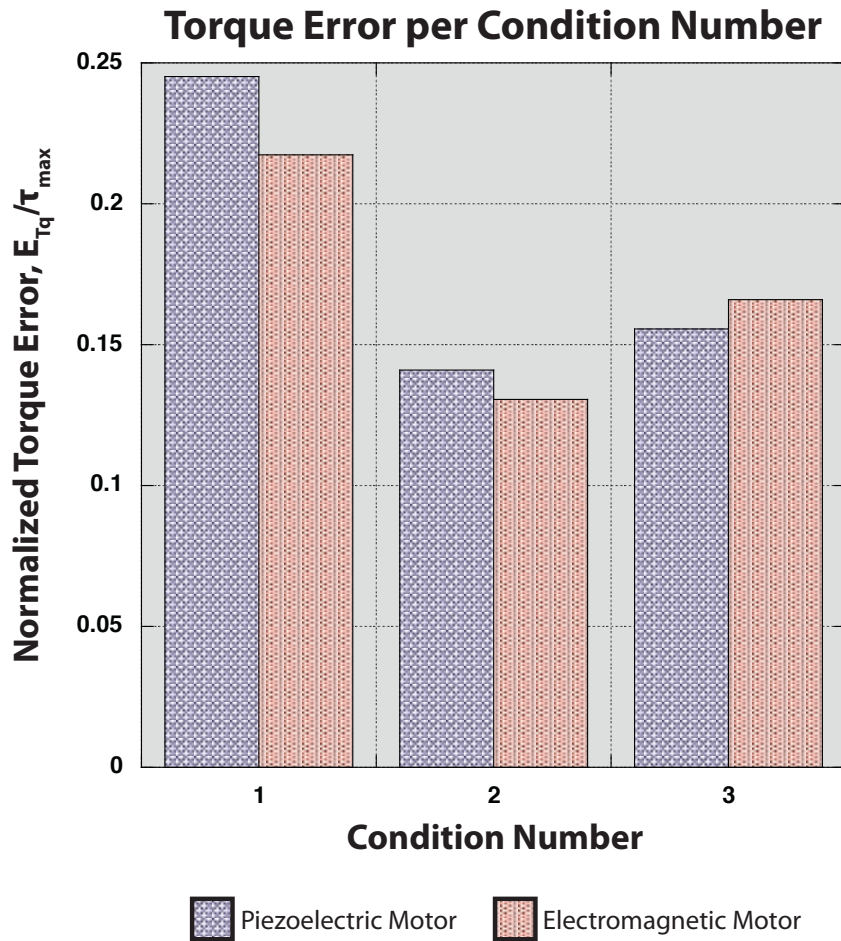


Figure 19: Torque error results per condition number

In the above bar graph (see Fig. 19), it is fairly clear that a minimum normalized torque error occurs in the second condition. As a reminder, this condition exemplifies the medium stiff spring (i.e. 900N/m) as well as the medium mass moment of inertia and torque magnitude. Although the third condition exhibits considerably less error than that of condition one, there is nevertheless a small positive slope from two to three. This is a curious result based on the fact that condition three scales to the biologically relevant spring via the allometric analysis, which was discussed in section 2.4.1. However, the following plot (see Fig. 20) does lend insight to this phenomenon.

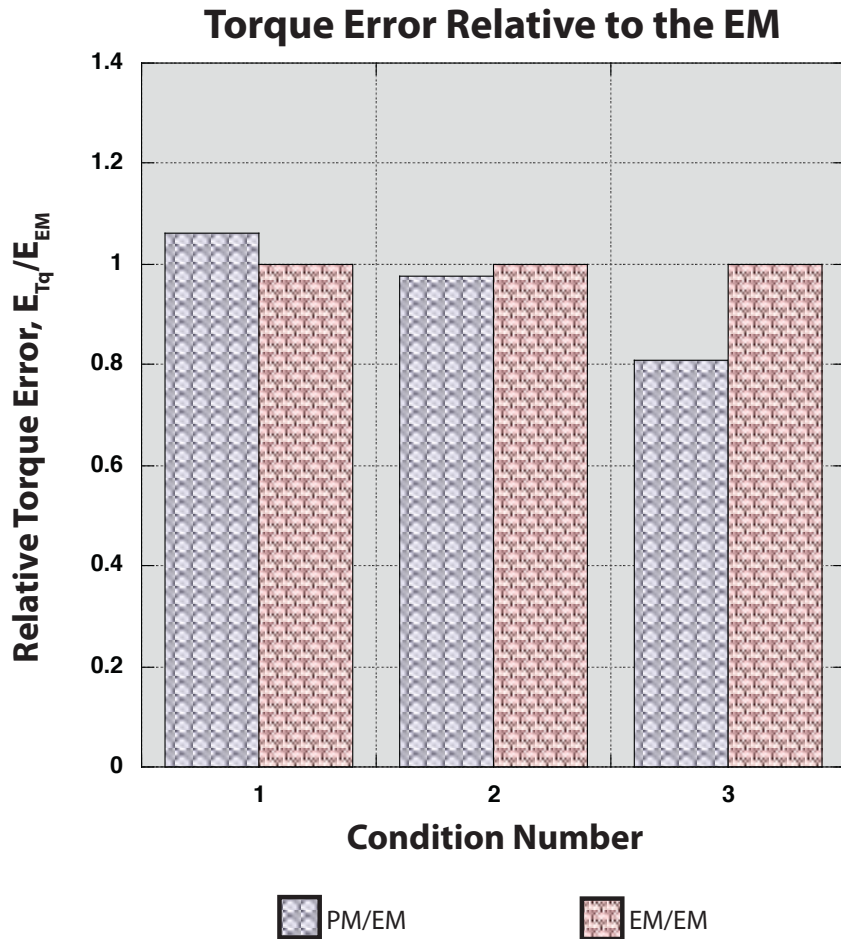


Figure 20: Torque error results relative to the EM



First, it should be noted that that the red bars in the bar graph represent the torque error data relative to itself. As a result, every value is exactly one. These bars are merely included in the plot as a visual reference for the blue bars, which represent the average torque error of the piezoelectric motors (PM) divided by the average torque error of the electromagnetic motors (EM). In this way, trends of the error in both motors can be explored through all three condition numbers. Specifically, it is observable that the PMs tend to perform more favorable in the higher condition numbers, relative to the performance of the EMs. It was already shown in previous plots (see Fig. 19) that condition two was the most optimal condition number. However, in relative terms, the PMs perform better than the EMs. Another way to phrase this phenomenon is that although both motors perform worse in condition three than they do in condition two, the PMs perform less worse than the EMs in condition three.

This result represents a proverbial silver lining amidst the general lackluster performance of the piezoelectric motors. Basically, it shows that the PMs are potentially better suited for biomimetic applications, possible as a result of their muscle-like ratcheting operation. Because it has been shown that the PMs tend to fair better in condition three than the EMs, this result was deemed worthwhile to continue exploring its effect in further detail. Additionally, the fact that condition three comprises of the most biologically relevant conditions, specifically with respect to elasticity, qualifies it for further investigation.

### 3.2.4 Trends at Biological Relevance

At the outset of this research, it was determined that biomimetics should serve as a fundamental point of focus for testing the actuators (e.g. PMs and EMs). Thus, additional analysis was performed specifically on the results of condition three with an emphasis on statistical analysis in order to tease apart the significance of the data. The following plot (see Fig. 21) compares normalized torque error in both motors at condition three over the relative frequency domain.

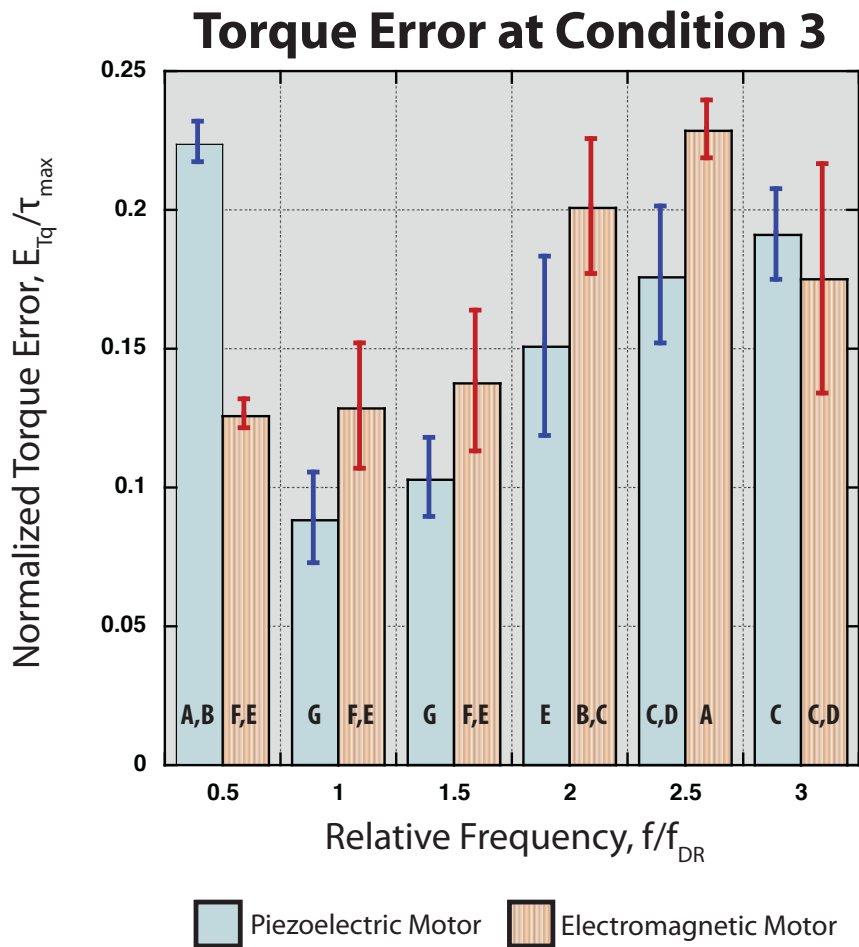


Figure 21: Torque error results at condition three

Although a general minimum of error can be found at resonance (i.e.  $f_{rel} = 1$ ), the standard deviation of the surrounding bars contributes to the subtle ambiguity of the data. In other words, the letters in bold and found at the bottom of each bar plot represent a lack of statistical significance via the associated bars labeled by the same letter. For example, the normalized torque error of the electromagnetic motor at relative frequencies 0.5, 1.0 and 1.5Hz are all labeled with an “E.” This indicates that there is no statistical significance between these values per the results of a statistical evaluation performed with JMP 7 statistical analysis software.

Regardless of similarities in data as a result of error propagating ambiguity, it is plainly observed that error increases toward the high end of the relative frequency domain. Additionally, error is particularly high for the piezoelectric motor at the lowest input frequency. As was already explained in prior sections, this is possibly an adverse result of the PM being favorable to very fast control frequencies. Thus, the limitations of a 50Hz controller are exaggerated in the case of a very slow input frequency.

Another trait of the above dataset (see Fig. 21) indicates that the piezoelectric motor seems to outperform the electromagnetic motor at most frequencies. The following figure (see Fig. 22) examines the trend(s) of efficiency for both motors under condition three.

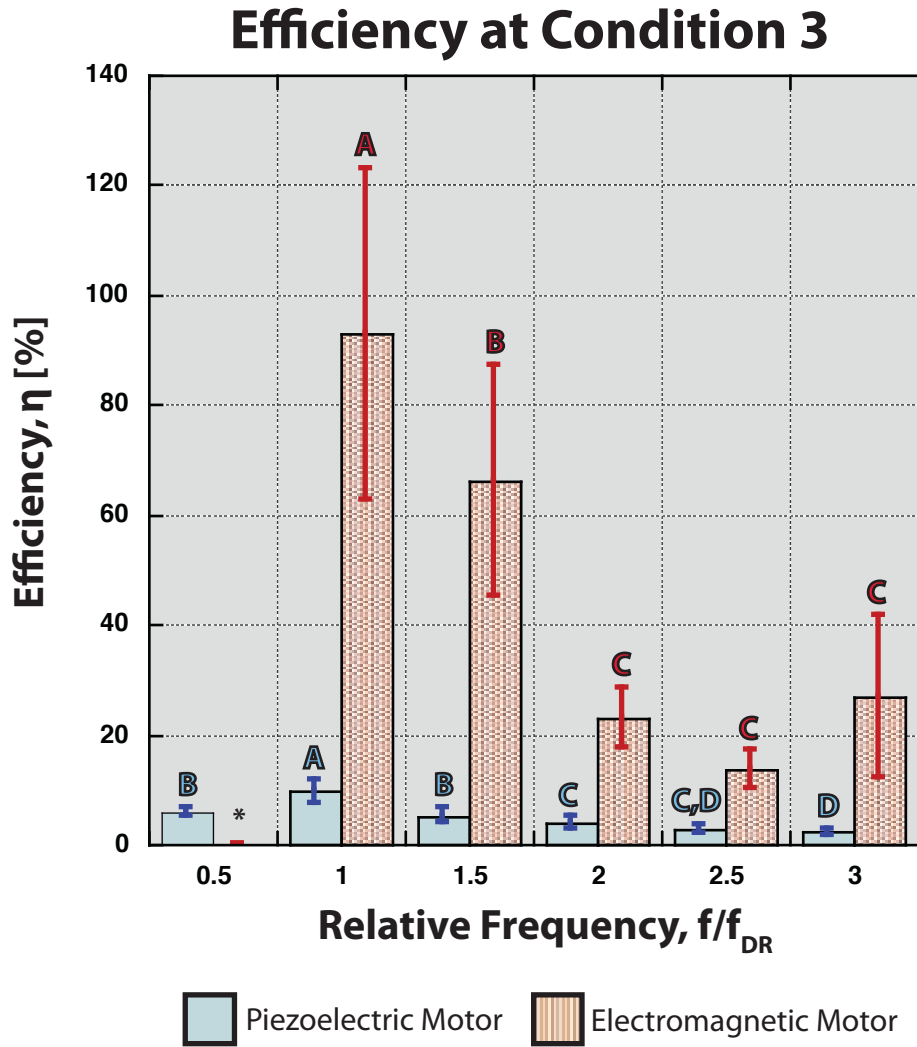


Figure 22: Efficiency results at condition three

In the above plot, efficiency is shown with a similar statistical analysis performed in the earlier torque error plot. The letters above the error bars represent the significance of the data within each particular motor's data. It should be noted that no data is reported at the lowest input frequency for the electromagnetic motor type due to current

measurements, which were too low to guarantee a fair reading of electrical consumption (\*).

Although the data clearly show a maximal efficiency for both motor types at resonance, the electromagnetic motors exhibit a very robust efficiency profile, which overshadows the efficiency performance of the piezoelectric motors. This point is particularly curious, given that PM are well known to be ultra-efficient motors. However, a sensitive oscillation may be to blame for such shortcomings.

As has already been mentioned in this document, the piezoelectric motors used in this study maintain an inherently profound response time several orders of magnitudes faster than that of electromagnetic motors. Although this should be a benefit, it is interpreted of the resulting data presented in this document that the ultra-fast response time of the PMs has acted as a metaphorical shackle holding back the promise of superior performance. In other words, it is believed that the sensitive response at the controller input of the PMs results in an exaggerated controller response to error. This ultimately results in a harsh overshoot that triggers the actuator into a fit of oscillations about the set point. The EMs, on the other hand, do not exhibit this behavior with such fervor. Instead, the slower response time of the EMs, which is well matched to the controller frequency of 50Hz, allows for the EMs to respond more mutedly to error. Ironically, this leads to a better performance as the sensitivity of its response is well fit to the controller.

Although this is an issue, which could be addressed via a more refined focus on the individual controller systems of the individual actuator types, it was felt that this solution would not address the issue at heart. In robotics industry today, it is very

common to use extensive control systems in order to cover up the inherent limitations of actuators commonly used (e.g. bulk hydraulic systems in Boston Dynamics' Big Dog). Although many of these systems are extremely impressive and capable of wonderfully nimble dynamic tasks, the fact remains that credit is most prominently due to clever control schemes and intensive modeling applications. The actuators themselves are often a weak link in the design. Thus, it was decided early on that this research would not focus on utilizing in-depth control system in order to homogenize a superior performance out of both the PMs and EMs. Instead, a common and capable controller was implemented to both actuator types with very little nuance and intentionally. In this way, it was hoped that some of the more fundamental limitations as well as beneficial traits would come out more clearly in the data.

It should also be noted that the distinct difference between the piezoelectric motors and the electromagnetic motors in terms of their response time lie their capacitive input impedance (i.e. capacity nano-farads) as opposed to the inductive input impedance of electromagnetic motors (i.e. milli-henries). Also, it is an unfortunate artifact of the equipment used for testing, that a 50Hz controller frequency was the fastest frequency that the processor could handle in Labview before missing data points. Barring these hardware limitations, it is clear that an increase in controller frequency would initially benefit both actuator types in terms of performance. However, it is hypothesized that no matter the sophistication of the controller used, eventually increasing the controller frequency by enough will result in a plateau of EM performance while the PMs will continue and possibly surpass the relative bench mark between actuators. Regardless, this

study inevitably resulted in forthcoming of just how important the controller frequency is in order to showcase the benefits of an ultra-fast actuator.

## **Chapter 4: Conclusions and Future Work**

### **4.1 Conclusions**

#### **4.1.1 Robotic Testing Platform**

The nature of the research described in this document has accumulated an appreciable value of knowledge, both in the form of biomimetic design, as well as actuator mechanics. The first iteration of a procedural strategy now exists for the design of a biomimetic test platform for artificial muscles in a series-elastic co-contractive system. Potentially, any type of rotary motor or linear actuator could be tested within the AMTS for a useful performance comparison.

#### **4.1.2 Performance Evaluation of Actuators**

There was significant indication in the data that condition two showed promise as an optimal vehicle for error minimization among both motor types. Even though condition three also performed well as the biological relevant condition, the first condition showed the worst performance out of the three.

Although the piezoelectric motor types failed to show performance improvements relative to electromagnetic motors across the board, there were significant instances showing potential (e.g. favorable performance indications at condition three). Additionally, a significant source of limitation has been identified in the form of a slow controller frequency, relative to the response time of PMs in particular.



## 4.2 Future Work

The most luring temptation for continuing work on this research includes the implication of an ultra-fast controller (kHz) in order to take full advantage of the fast response time inherent to the piezoelectric motor's design. Regardless, there are many other directions the research could be taken in as well.

One particular way forward on the research may also include the development of a more sophisticated controller including in-depth modeling for each of the motor types. Although this modeling could prove tricky, specifically for the piezoelectric motors, the certain complexity of the task may prove to be worthwhile in overcoming some of the limitations of each motor type. As was discussed in this document, one of the downsides of this could be that overly competent controllers tend to mask some of the inadequacies of actuator systems by artificially increasing their competency in dynamic systems. This was one of the original rationales for limiting the controller(s) of this project to a very simple system capable of accomplishing utility without necessarily exceeding. In this way, it was hoped that the flaws of the physical actuators would shine through for a clearer and more pure comparison. However, it may be worth a second consideration for future work, in order to optimize the performance(s) of both motor types. This may indeed result in a very different outcome than that which was found in the studies currently completed.

Another direction for future work with respect to the AMTS could focus more on the design aspects of the whole system. Utilizing multiple motors in parallel and in series could provide an interesting insight on the biomimetics of muscle fiber orientation in terms of trading increased velocity for increased torque production and vice versa.

Another way to incorporate more biomimetic design would be to find a method for increasing torque production past maximum values in the eccentric contraction phase.

Yet another area of future focus could include further experimentation with increased co-contraction as well as impedance control for perturbation rejection. These concepts were touched upon in the current iteration of this project, however they could be explored much more thoroughly in future research.

Finally, it would be rewarding to begin incorporating the AMTS design as a subsystem of a larger system such as an entire robotic leg or even a whole robotic organism. Another example for future application could potentially be a prosthetic joint such as an artificial ankle or knee. It would be very informative to observe the performance of the AMTS as an actuator in a larger system, more dynamically complex system.

## Appendix: Sample Data

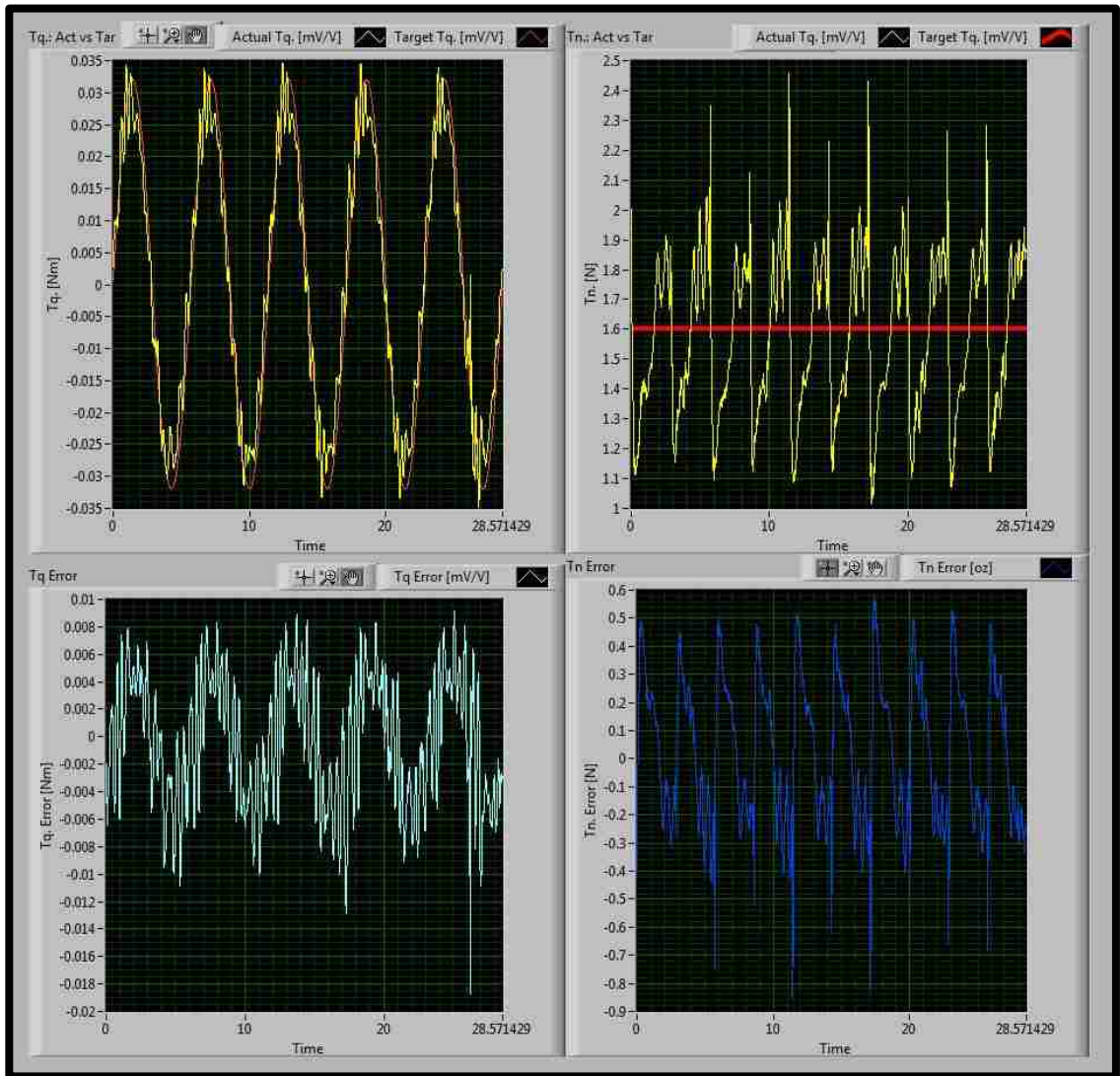


Figure 23: Sample data of the electromagnetic motor at condition three

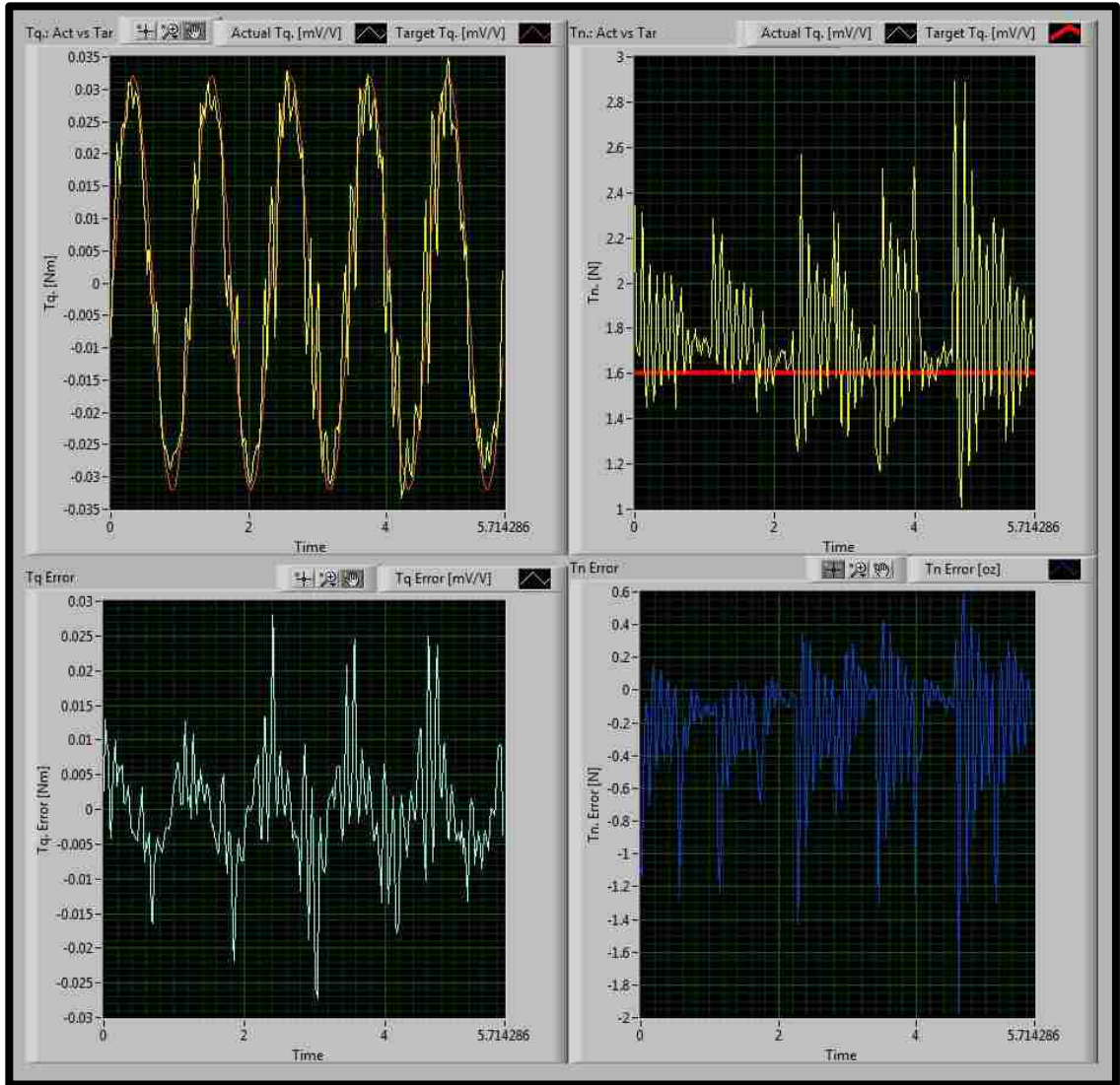


Figure 24: Sample data of the piezoelectric motor at condition three

## Bibliography

- Anderson, N.E. and Loewenthal, S.H. (1980). Spur-Gear-System Efficiency at Part and Full Load. NASA Technical Paper 1622 (February), 79-46.
- Conway, B.A., Hultborn, H. and Kiehn, O. (1987). *Experimental Brain Research*. 68. 643-656. (July).
- Flynn, A.M., Tavrow, L.S., Bart, S.F. and Brooks, R.A. (1992). Piezoelectric Micromotors for Microbots. *Journal of Microelectromechanical Systems*. 1(1), 44-51. doi:1057-7157/92503.00
- Hedrick, T.L. (2008). Software techniques for two- and three-dimensional kinematic measurements of biological and biomimetic systems. *Bioinspiration and Biomimetics*. doi: 10.1088/1748-3182/3/3/034001
- Hollerbach, J.M., Hunter, I.W. and Ballantyne, J. (1991). A Comparative Analysis of Actuator Technologies for Robotics. *Robotics Review*.
- Klute, G.K., Czerniecki, J.M. and Hannaford, B. (1999). McKibben Artificial Muscles: Pneumatic Actuators with Biomechanical Intelligence. *IEEE/ASME International Conference on Advanced Intelligent Mechatronics*. (September 19-22).
- Krishnan, R. and Pillay, P. (1987). Modeling, simulation, and analysis of permanent-magnet motor drives part II: the brushless DC motor drive. *IEEE Interactions on Industry Applications*. 25(2), 274-279. doi:10.1109/28.25542
- Pollock, C.M. and Shadwick, R.E. (1994). Allometry of muscle, tendon, and elastic energy storage capacity in mammals. *American Journal of physiology; regulatory, integrative and comparative physiology*. 266(3), 1022-31.
- Pollock, C.M. and Shadwick, R.E. (1994). Relationship between body mass and biomechanical properties of limb tendons in adult mammals. *American Journal of physiology; regulatory, integrative and comparative physiology*. 266(3), 1016-21.
- Pratt, G.A., Williamson, M.M., Dillworth, P., Pratt, J.E., Ulland, K. and Wright, A. (1995). Stiffness Isn't Everything. *Preprints of the Fourth International Symposium on Experimental Robotics*. (June 30 – July 2).
- Pratt, J.E. and Krupp, B.T. (2004). Series Elastic Actuators for legged robots. *Unmanned Ground Vehicle Technology VI*. 135. doi:10.1117/12.548000.
- Robinson, D.W., Pratt, J.E., Paluska, D.J. and Pratt, G.A. (1999). Series Elastic Actuator Development for a Biomimetic Walking Robot. *IEEE/ASME International Conference on Advanced Intelligent Mechatronics*. (September 19-22).

- Sun, D., Lie, J. and Ai, X. (2002). Modeling and performance evaluation of traveling-wave piezoelectric motors with analytical method. *Sensors and Actuators A*. 100, 84-93. doi: 10.1016/S0924-4247(02)00151-6
- Tondu, B. (2012). Modeling of the McKibben artificial muscle: A review. *Journal of Intelligent Material Systems and Structures*. 23(3), 225-253. doi: 10.1177/1045389X11435435.
- Uchino, K. (1997). Piezoelectric Actuators and Ultrasonic Motors. Kluwer Academic Publishers. Norwell, Massachusetts 02061 USA.
- Veneman, J.F., Ekkelenkamp, R., Kruldhof, R., van der Helm, F.C.T. and van der Kooij, H. (2006). A Series Elastic- and Bowden-Cable-Based Actuation System for Use as Torque Actuator in Exoskeleton-Type Robots. *The International Journal of Robotics Research*. 25(261), 261-281. doi: 10.1177/0278364906063829
- Yeadon, M.R., King M.A., Forrester, S.E., Caldwell, G.E. and Pain, M.T.G. (2010). The need for muscle co-contraction prior to landing. *Journal of Biomechanics*. 364-369. doi:10.1016/j.biomech.2009.06.058.
- Ziegler, J.G. and Nichols, N.B. (1942). Optimum settings for automatic controllers. *Transactions of the A.S.M.E.* 759-765.

# Curriculum Vitae

**Ryan Schroeder**

4200 Paradise Rd. #2077 Las Vegas, Nevada 89169  
T: (760) 900-4716 E: schroe95@unlv.nevada.edu

I plan to develop a career in Biomechanical Engineering so that I may use this knowledge to integrate robotic systems with biological systems intended for the purpose of assisting disabled peoples as well as enhancing general human performance. I ultimately plan on achieving a Doctoral degree in the above-specified field.

## Teaching Assistant

*Spring '14 to Present*

- Working at the engineering tutoring center at UNLV to help undergraduate students with fundamental course work such as statics and dynamics.
- Teaching the fluids mechanics lab with a focus on fundamental experiments relevant to fluid properties, hydrostatic pressures, laminar flows and friction losses in a pipe
- Awarded "Teaching Assistant of the Year" for the Mechanical Engineering Department at the University of Nevada, Las Vegas for the academic school year of 2013-2014.

## Research Assistant – Lab of Comparative Biomechanics

*Fall '12 to Present*

- Researching the potential of piezoelectric motors to outperform electromagnetic motors in the context of biomechanical systems such as prosthetics or exoskeletons
- Designed and built an artificial musculotendon system capable of biomimetic function with respect to operating principles such as neural motor control, antagonistic flexor-extensor couples and impedance for improved force control
- Researching simulations of a quadruped robot by utilizing a predictive mathematical model to test parameter spaces for successful trotting gaits (collaboration with Dr. Mohamed Trabia)
- Working to extend the image processing capabilities of Matlab scripts for x-ray motion analysis

## Senior Design Project

*Fall '12 to Spring '13*

- Designed an ergonomic, thermo-regulated blanket for comfortable sleeping in regions having extreme temperature gradients
- Modeling, analysis and PowerPoint presentation for project objective, analysis and results
- Bill of Materials, ordering parts and building a working prototype

## Conference Abstract

- Schroeder, R. T. and Lee, D. V. (2014). Piezoelectric Versus Electromagnetic Series Elastic Actuators for Muscle-Tendon Systems. *Integrative and Comparative Biology*.

University of Nevada, Las Vegas  
**M.S. in Mechanical Engineering, Specialty in Dynamics and Controls**

*Summer '13 to Present*

- Cumulative GPA: 4.00
- Dean's List for *all* semesters present
- Multiple projects as a research assistant in Dr. David Lee's Lab of Comparative Biomechanics (LoCB)
- Relevant Coursework: Advanced Dynamics, Human Motor Control, Robotics, Comparative Vertebrate Anatomy and Biomechanics, Transport Phenomenon in Humans

University of Nevada, Las Vegas  
**Mechanical Engineering and Integrated B.S./M.S. Program**

*Summer '10 to Spring '13*

- Cumulative GPA: 3.83
- Dean's List for *all* semesters present
- Member of Tau Beta Pi Honors Society and ASME
- Member of Phi Kappa Phi Honors Society
- Relevant Coursework: Automatic Controls, Vibrations, Machine Component Design, Dynamics of Machines, Biomechanics, Material Mechanics, Special Lectures – Biomechanics of Perturbed Gait, Dynamic Systems Modeling and Analysis, Measurements

Musician's Institute  
**Music Performance, Piano and Keyboards**

*Fall '07 to Spring '08*

- Cumulative GPA: 3.86
- Coursework: Music Theory, Technique, Voicings, Sight Reading, Music Style and History, Band, Conducting and Arranging.

Victor Valley Community College  
**Associates Degree in Fine Arts, General Education**

*Fall '05 to Spring '07*

- Cumulative GPA: 3.82
- Graduated with High Honors
- Coursework: College Algebra, Earth Sciences, Human Biology and Anatomy, Psychology, Music Appreciation and Theory.